

Intensity and anisotropies of the stochastic Gravitational Wave background from merging compact binaries in galaxies

Giulia Capurri,^{a,b,c} Andrea Lapi,^{a,b,c,d} Carlo Baccigalupi,^{a,b,c}
Lumen Boco,^{a,b,c} Giulio Scelfo,^{a,b,c} Tommaso Ronconi^{a,b,c}

^aSISSA, via Bonomea 265, 34136, Trieste, Italy

^bINFN, Sezione di Trieste, via Bonomea 265, 34136, Trieste, Italy

^cIFPU, via Beirut 2, 34151, Trieste, Italy

^dINAF/OATS, via Tiepolo 11, I-34143 Trieste, Italy

E-mail: giulia.capurri@sissa.it, andrea.lapi@sissa.it, carlo.baccigalupi@sissa.it,
lumen.boco@sissa.it, giulio.scelfo@sissa.it, tommaso.ronconi@sissa.it

Abstract. We investigate the isotropic and anisotropic components of the Stochastic Gravitational Wave Background (SGWB) originated from unresolved merging compact binaries in galaxies. We base our analysis on an empirical approach to galactic astrophysics that allows to follow the evolution of individual systems. We then characterize the energy density of the SGWB as a tracer of the total matter density, in order to compute the angular power spectrum of anisotropies with the Cosmic Linear Anisotropy Solving System (CLASS) public code in full generality. We obtain predictions for the isotropic energy density and for the angular power spectrum of the SGWB anisotropies, and study the prospect for their observations with advanced Laser Interferometer Gravitational-Wave and Virgo Observatories and with the Einstein Telescope. We identify the contributions coming from different type of sources (binary black holes, binary neutron stars and black hole-neutron star) and from different redshifts. We examine in detail the spectral shape of the energy density for all types of sources, comparing the results for the two detectors. We find that the power spectrum of the SGWB anisotropies behaves like a power law on large angular scales and drops at small scales: we explain this behaviour in terms of the redshift distribution of sources that contribute most to the signal, and of the sensitivities of the two detectors. Finally, we simulate a high resolution full sky map of the SGWB starting from the power spectra obtained with CLASS and including Poisson statistics and clustering properties.

Contents

| | | |
|----------|---|-----------|
| 1 | Introduction | 1 |
| 2 | Astrophysical sources | 3 |
| 3 | Anisotropic stochastic Gravitational Wave background | 5 |
| 3.1 | Isotropic SGWB | 5 |
| 3.2 | SGWB anisotropies | 7 |
| 4 | Results | 9 |
| 4.1 | Energy density of the astrophysical SGWB | 9 |
| 4.2 | Characterizing the SGWB as a tracer of matter | 10 |
| 4.3 | Angular power spectrum of SGWB anisotropies | 14 |
| 4.4 | SGWB anisotropy sky map | 17 |
| 5 | Conclusions | 20 |

1 Introduction

The discovery of Gravitational Waves (GWs) by the advanced Laser Interferometer Gravitational - Wave and Virgo Observatories (aLIGO/Virgo) collaboration [1–8] has opened a new observational window on the Universe. We are currently in the third observing run (O3) and a large number of new GW events from binary black hole (BH-BH), neutron star (NS-NS), and black hole-neutron star (BH-NS) mergers is being detected [9–13]. Together with the observation of single events, the detection and characterization of the Stochastic Gravitational Wave Background (SGWB) from unresolved compact binary coalescences is one of the most challenging targets for the GW community. The search for the isotropic SGWB using the O3 data, combined with upper limits from the earlier O1 and O2 runs [14, 15], constrains its energy density to be $\Omega_{\text{gw}} < 5.8 \times 10^{-9}$ at 25 Hz with 95% confidence for a flat SGWB and $\Omega_{\text{gw}} < 3.4 \times 10^{-9}$ for a power law SGWB with a spectral index of 2/3, consistently with expectations for compact binary coalescences [16]. Likewise, within current uncertainties, the data are consistent with an isotropic SWGB [17, 18].

The phenomena that can produce a SGWB can be classified with respect to their astrophysical or cosmological origin (see [19] for a general review). The astrophysical SGWB is constituted by the incoherent superposition of signals from of a large number of unresolved astrophysical sources, including merging double compact objects, merging supermassive black holes binaries [20, 21], core collapse supernovae [22–24], rotating neutron stars [25–27] and population III binaries [28]. On the other hand, cosmological contributions to the SGWB are primarily expected from the amplification of vacuum quantum fluctuations during inflation [29–32], but also from GWs produced during the reheating phase at the end of inflation itself [33–35]. Inflationary scenarios, also involving recently proposed models based on SU(2) symmetries, can be constrained from GWs observatories in conjunction with B-modes of the Cosmic Microwave Background observations [36]. Other, perhaps more exotic, cosmological sources of GWs are pre-Big Bang scenarios [37–39], cosmic strings [40–42], primordial black holes [43–45], first-order phase transitions in the early universe [46–49] and magnetic fields

[50, 51]. The different backgrounds contribute at different frequencies and have distinct statistical properties, so that their characterization potentially allows to distinguish them from possible future detections.

The SGWB will be scrutinized by powerful observatories in the forthcoming years and decades. The current generation of ground-based laser interferometers (LIGO [52], Virgo [53], the Kamioka Gravitational Wave Detector, KAGRA, [54]) will be succeeded by Einstein Telescope (ET) [55–59] and Cosmic Explorer (CE) [60], both operating between a few Hertz and a few kilo-Hertz. The Laser Interferometer Space Antenna (LISA) is scheduled for observations in the early 2030s, targeting a variety of SGWB sources in the milli-Hertz band (see e.g. [61, 62] and references therein). Other proposals for future space missions include μ Ares [63] in the micro-Hertz band; the Advanced Millihertz Gravitational-wave Observatory (AMIGO) [64] in the milli-Hertz band; the Big Bang Observer (BBO) [65, 66], the Deci-hertz Interferometer Gravitational wave Observatory (DECIGO) [67, 68], the Decihertz Observatory (DO) [69] and the Atomic Experiment for Dark Matter and Gravity Exploration in Space (AEDGE) [70] in the deci-Hertz band. Finally, current generation of pulsar timing arrays (PTA) experiments, such as the Nanohertz Observatory for Gravitational Waves (NANOGrav) [71], the European PTA [72] and the Parkes PTA [73] are placing limits on the SGWB in the nano-Hertz band. In the next future, also Square Kilometre Array (SKA) [74] will join this international network of PTA.

The SGWB produced by merging Double Compact Objects (DCOs) in galaxies is expected to be one of the dominant contributions to the total background. Its characterization is complex since it requires to model many astrophysical and cosmological processes occurring on different times and spatial scales: from stellar physics, through galaxy formation and evolution, up to GW physics and evolution of cosmological perturbations. On the other hand, the information richness encoded in the SGWB produced by merging DCOs makes its detection and characterization one of the main goals of GW experiments. For this reason, knowing how this background is related to astrophysical models and parameters will be of paramount importance for improving our understanding of such astrophysical processes once the SGWB will be detected. Moreover, a high precision modelling of the SGWB from astrophysical sources is needed in order to measure other components of the background, as the primordial one expected from cosmic inflation.

The isotropic component of the SGWB produced by merging DCOs has been computed in many works (e.g. [75–83]), according to different prescriptions for stellar and galactic physics. In particular, these studies typically combine population synthesis either with cosmological simulations or with recipes on the cosmic star formation rate density and metallicity distributions inferred from observations. For what concerns the anisotropies of the astrophysical SGWB, their first theoretical expression was derived in [84, 85]. Predictions for the angular power spectrum of the anisotropies based on this expression have been presented in [86–89], where the influence of various astrophysical models on the power spectrum was also investigated. Based on the same framework, at least two other approaches have been proposed to compute the anisotropies of the astrophysical SGWB. One of them is treated in [90, 91] and the related results for the angular power spectrum are discussed in [92–94]. A third approach was presented in [95], where a new derivation of the SGWB anisotropies in a cosmological context is proposed: in this work, the observed angular power spectrum is computed accounting for all the projection effects intervening between the source and the observer. All the aforementioned results concerning the SGWB anisotropies are compared in a recent work [96]. There, the authors show that the predictions are basically all equivalent

and that they all contain the same well-known cosmological effects, so that differences in predictions can only arise in the way galactic and sub-galactic physics is computed.

In the present paper, we focus on the isotropic and the anisotropic components of the SGWB produced by merging DCOs in galaxies as possibly detected by aLIGO/Virgo and in the future by the ET. Our analysis is built on an empirical approach to galactic astrophysics, which allows to follow the evolution of individual systems [97–99]. We compute the power spectrum of the SGWB anisotropies in full generality with the public code CLASS, exploiting the formalism similarities between galaxy number counts and SGWB [100, 101]. In order to do so, we characterize the energy density of the SGWB as a tracer of matter density. Finally, we develop a methodology to simulate a stochastic realization of the full-sky map of the SGWB, taking into account the intrinsic Poisson nature of the signal as well as its clustering properties.

The paper is structured as follows: in Section 2 we describe the physical prescriptions employed to describe the astrophysical sources; in Section 3 we summarize the theory behind the study of the SGWB, from the computation of the isotropic energy density to the formalism behind the calculation of the angular power spectrum of its anisotropies; in Section 4 we characterize the SGWB as a tracer of the matter density and we present our results for its amplitude and anisotropies; in Section 5 we draw our conclusions and outline future prospects. Throughout this work we adopt the standard flat Λ CDM cosmology with parameter values from the Planck 2018 legacy release [102], with Hubble rate today corresponding to $H_0 = 67.4 \text{ km s}^{-1} \text{ Mpc}^{-1}$, Cold Dark Matter (CDM) and baryon abundances with respect to the critical density corresponding to $\Omega_{\text{CDM}}h^2 = 0.120$ and $\Omega_b h^2 = 0.022$, respectively, reionization optical depth $\tau = 0.054$, amplitude and spectral index of primordial scalar perturbations corresponding to $\ln(10^{10} A_S) = 3.045$ and $n_S = 0.965$, respectively.

2 Astrophysical sources

In this work we focus on the SGWB produced by the superposition of GW signals coming from a particular class of astrophysical sources: Double Compact Object (DCO) merging binaries. The large amount of astrophysical and cosmological information that it encodes, together with the fact that it is expected to be the dominant component of the total SGWB, makes the modelling of this component of the astrophysical SGWB of great scientific interest. In the characterization of the population of DCOs and in the computation of their merging rates, we follow the approach presented in [97–99], which is briefly sketched hereafter. The merging rate per unit volume V and chirp mass \mathcal{M}_c can be computed as:

$$\frac{d\dot{N}}{dV d\mathcal{M}_c}(t) = \int dt_d \int dZ \frac{dN}{dM_{\text{SFR}} d\mathcal{M}_c dt_d}(Z) \frac{dM_{\text{SFR}}}{dV dZ}(t - t_d), \quad (2.1)$$

where t is the cosmic time, equivalent to redshift, M_{SFR} is the stellar mass associated to the Star Formation Rate (SFR), t_d is the delay time between the formation of the progenitor binary and the merging of the compact objects binary, Z is the galaxy metallicity and V the comoving volume. The first term in the integral is related to stellar and binary evolution and represents the number of DCO mergers per unit of star forming mass per bin of chirp mass and time delay. It can be decomposed into three factors:

$$\frac{dN}{dM_{\text{SFR}} d\mathcal{M}_c dt_d}(Z) = \frac{dN}{dM_{\text{SFR}}}(Z) \frac{dp}{d\mathcal{M}_c}(Z) \frac{dp}{dt_d}, \quad (2.2)$$

where dN/dM_{SFR} is the number of merging DCOs per unit of mass formed in stars at metallicity Z , dp/dM_c is the metallicity-dependent chirp mass distribution and dp/dt_d is the normalized distribution of delay times between the formation of the progenitor binary and the merger. The latter quantity is found to be $\propto t_d^{-1}$ with $t_{d,\text{min}} \sim 50$ Myr by various authors independently on metallicity or DCO type [103–105]. For the former two factors, we rely on the results of the STARTRACK population synthesis simulations¹, ‘reference B’ model in [103, 106]. In the present work, we separate the contribution to the merging rates coming from the 3 different types of DCO mergers: BH-BH, NS-NS and BH-NS.

The second term in the integral of equation (2.1) is instead related to galaxy evolution and represents the star forming mass per unit time, comoving volume and metallicity. In the present work, we compute it using observationally derived prescriptions. In particular, following the procedure depicted in [99], we exploit the Star Formation Rate Functions (SFRF) as galaxy statistics and the Fundamental Metallicity Relation (FMR) to assign metallicity to galaxies. The SFRF $dN/d\log\psi/dV$ represents the galaxy number density per logarithmic bin of SFR at different redshifts and have been derived in [107] from the galaxy Ultra-Violet (UV), Infra-Red (IR), submm, and radio luminosity functions at different redshift. The gas phase metallicity Z of the interstellar medium, instead, is derived through the empirical FMR, see e.g. [108–111], which is a three parameter relation among the stellar mass of the galaxy M_\star , SFR, and Z . Since galaxies are parametrized and counted through the SFRF statistics, we need to relate the SFR to M_\star in order to derive a metallicity. We do it through the main sequence of star forming galaxies, an observational redshift dependent power law relationship between the stellar mass and the SFR (see e.g. [112–118]). Even though the main sequence is a relation followed by most of the star forming objects, there is a non negligible population of galaxies, called starbursts, which lies above the main sequence: their SFR is higher with respect to the SFR predicted by the main sequence at a given mass. In order to model this population, we follow [99] that provides a M_\star distribution $dp/dM_\star(M_\star|z, \psi)$ for galaxies at fixed value of SFR.

With all these ingredients, we can compute the galactic term of equation (2.1) as:

$$\frac{d\dot{M}_{\text{SFR}}}{dV dZ}(Z|z) = \int d\log\psi \psi \frac{dN}{dV d\log\psi} \int dM_\star \frac{dp}{dM_\star}(M_\star|z, \psi) \frac{dp}{dZ} \Big|_{\text{FMR}}(Z|Z_{\text{FMR}}(M_\star, \psi)), \quad (2.3)$$

where $dp/d\log Z|_{\text{FRM}} \propto \exp[-(\log Z - \log Z_{\text{FMR}}(M_\star, \psi))^2/2\sigma_{\text{FMR}}^2]$ is a log normal distribution around the logarithmic metallicity value set by the FMR at fixed stellar mass and SFR.

The resulting merging rates are shown in figure 1. These are found to be in good agreement with the recent local determination by the LIGO/Virgo collaboration, as shown in [99], but since the uncertainties of both the galactic and the stellar terms are huge, we decide to re-normalize our results to match the local merging rates values of the latest LIGO/Virgo estimations: $23.9_{-8.6}^{+14.9} \text{ Gpc}^{-3} \text{ yr}^{-1}$ for BH-BH and $320_{-240}^{+490} \text{ Gpc}^{-3} \text{ yr}^{-1}$ for NS-NS [119]². For BH-NS events there is only an upper limit of $610 \text{ Gpc}^{-3} \text{ yr}^{-1}$ and therefore we use the results without any re-normalization.

Finally, we stress that our method to compute the merging rates presents a twofold benefit: on the one hand the galactic part is completely observational based, not relying on the results of any cosmological simulation or semi-analytic framework; on the other hand,

¹We use the simulation data publicly available under this url: <https://www.syntheticuniverse.org/>

²Note that we normalize to the mode value given by LIGO/Virgo.

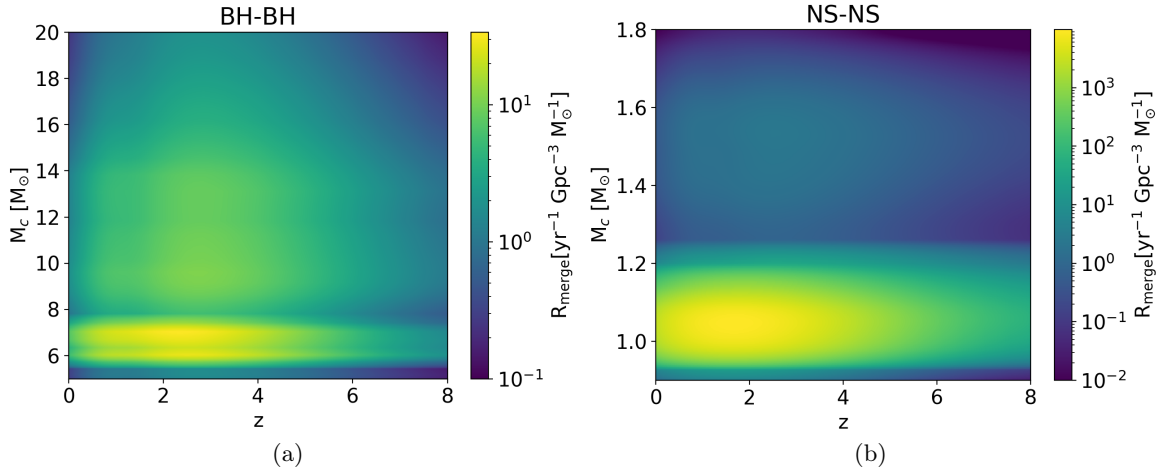


Figure 1: Differential merging rates $d\dot{N}/dV d\mathcal{M}_c$ as a function of redshift and chirp mass for BH-BH (a) and NS-NS (b) events. Notice that in both cases the greatest contribution come from $z \sim 2-3$, but NS-NS rates are around two order of magnitude higher than BH-BH ones.

making use of the SFR functions as galaxy statistics, we are able to assess the contribution of galaxies with different properties to the overall DCO merging rate.

3 Anisotropic stochastic Gravitational Wave background

The spectrum of the SGWB is characterized by the dimensionless energy density parameter

$$\Omega_{\text{gw}}(f_o, \hat{e}_o) = \frac{1}{\rho_c} \frac{d^3 \rho_{\text{gw}}(f_o, \hat{e}_o)}{d \ln f_o d^2 \sigma_o} = \frac{8\pi G f_o}{3H_0^2 c^2} \frac{d^3 \rho_{\text{gw}}(f_o, \hat{e}_o)}{df_o d^2 \omega_o}, \quad (3.1)$$

where $\rho_c = 3H_0^2 c^2 / 8\pi G$ is the critical density and ρ_{gw} is the SGWB energy density at the observed frequency f_o , arriving from a solid angle ω_o centred on the observed direction \hat{e}_o . This quantity can be split into a homogeneous and isotropic term $\bar{\Omega}_{\text{gw}}(f_o)$ and a directional dependent GW energy density contrast $\delta\Omega_{\text{gw}}(f_o, \hat{e}_o)$:

$$\Omega_{\text{gw}}(f_o, \hat{e}_o) = \frac{\bar{\Omega}_{\text{gw}}(f_o)}{4\pi} + \delta\Omega_{\text{gw}}(f_o, \hat{e}_o). \quad (3.2)$$

The term $\bar{\Omega}_{\text{gw}}/4\pi$ corresponds to the average GW flux per unit solid angle at the frequency f_o , whereas $\bar{\Omega}_{\text{gw}}$ is the total GW flux. Since in literature results for isotropic models of the SGWB are usually expressed in terms of the total flux, we are going to express our results in terms of $\bar{\Omega}_{\text{gw}}$. The aim of this Section is to explain how we compute the above isotropic and anisotropic terms.

3.1 Isotropic SGWB

The isotropic component of the SGWB is constituted by the superposition of all the unresolved GW signals from coalescing compact binaries in galaxies. The intensity of such signals depends on the chirp mass and redshift of the source binary. In fact, the typical waveform of a GW from a binary system is proportional to:

$$\tilde{h}(g) \propto \mathcal{M}_z^{5/6} D_L^{-1}(z) F(f), \quad (3.3)$$

where \mathcal{M}_z is related to the chirp mass \mathcal{M}_c through $\mathcal{M}_z = \mathcal{M}_c(1+z)$, $D_L(z)$ is the luminosity distance of the source and $F(f)$ is a frequency behaviour that depends on the phase of the orbital evolution and is usually described by post-Newtonian approximations. The isotropic energy density of the SGWB is hence directly related to the merger rates of binaries and to the energy spectrum of the GW signal generated by each source, but also to the sensitivity of the observing detector. Therefore, as with increasing detector sensitivity it will be possible to resolve a larger fraction of events out to higher redshift, the total intensity of the SGWB will be reduced.

All in all, the isotropic energy density of the SGWB is given by the following well known expression (see e.g. [75–83]):

$$\bar{\Omega}_{\text{gw}}(f_o) = \frac{8\pi G f_o}{3H_0^3 c^2} \int dz \int d\mathcal{M}_c \frac{R_{\text{merge}}(\mathcal{M}_c, z)}{(1+z) h(z)} \frac{dE}{df}(f_e(z)|\mathcal{M}_c) \int_0^{\bar{\rho}} d\rho P_\rho(\rho|\mathcal{M}_c, z), \quad (3.4)$$

where $R_{\text{merge}} = d\dot{N}/dVd\mathcal{M}_c$ is the intrinsic merger rate per unit comoving volume and per unit chirp mass, $h(z) = [\Omega_M(1+z)^3 + 1 - \Omega_M]^{1/2}$ accounts for the dependence of comoving volume on cosmology, dE/df is the energy spectrum of the signal emitted by a single binary evaluated in terms of the source frequency $f_e = (1+z)f_o$ and P_ρ is the distribution of signal-to-noise ratio (S/N) for a given detector at given chirp mass and redshift. The rationale behind the previous equation is to compute the energy density of the SGWB summing the contributions of all those GW events whose S/N is below the detection threshold $\bar{\rho} = 8$. Of course, the energy density of the SGWB produced by all the events, resolved and unresolved, can be easily obtained using $\bar{\rho} = \infty$ in equation (3.4): in this way, the S/N integral is equal to 1 and all the events are taken into account. Following the formalism depicted in [120, 121], we compute the distribution of S/N as

$$P_\rho(\rho|\mathcal{M}_c, z) = P_\Theta(\Theta_\rho) \frac{\Theta_\rho}{\rho}, \quad (3.5)$$

in terms of the orientation function

$$\Theta = \frac{\rho}{8} \frac{D_L(z)}{R_0} \left[\frac{1.2M_\odot}{(1+z)\mathcal{M}_c} \right]^{5/6} \frac{1}{\sqrt{\zeta_{\text{isco}} + \zeta_{\text{insp}} + \zeta_{\text{merg}} + \zeta_{\text{ring}}}}, \quad (3.6)$$

and its distribution function

$$P_\Theta = \begin{cases} 5\Theta(4-\Theta)^3/256 & 0 < \Theta < 4, \\ 0 & \text{otherwise} \end{cases}. \quad (3.7)$$

In the above expressions R_0 is the detector characteristic distance parameter given by

$$R_0^2 = \frac{5}{192} \sqrt{N_{\text{det}}} \frac{M_\odot^2}{\pi c^3} \left(\frac{3G}{20} \right)^{5/3} x_{7/3}, \quad (3.8)$$

where N_{det} is the number of co-located detectors and $x_{7/3}$ is the auxiliary quantity

$$x_{7/3} = \int_0^\infty \frac{df}{(\pi M_\odot)^{1/3} f^{7/3} S(f)}, \quad (3.9)$$

with $S(f)$ the noise spectral density. The functions ζ_{isco} , ζ_{insp} , ζ_{merg} and ζ_{ring} specify the overlap of the waveform with the observational bandwidth during the inspiral, merger and ring-down phases of the event and are given by:

$$\begin{aligned}
\zeta_{\text{isco}} &= \frac{1}{(\pi M_{\odot})^{1/3} x_{7/3}} \int_0^{2f_{\text{isco}}} \frac{df}{S(f)} \frac{1}{f^{7/3}}, \\
\zeta_{\text{insp}} &= \frac{1}{(\pi M_{\odot})^{1/3} x_{7/3}} \int_{2f_{\text{isco}}}^{f_{\text{merg}}} \frac{df}{S(f)} \frac{1}{f^{7/3}}, \\
\zeta_{\text{merg}} &= \frac{1}{(\pi M_{\odot})^{1/3} x_{7/3}} \int_{f_{\text{merg}}}^{f_{\text{ring}}} \frac{df}{S(f)} \frac{1}{f^{4/3} f_{\text{merg}}}, \\
\zeta_{\text{ring}} &= \frac{1}{(\pi M_{\odot})^{1/3} x_{7/3}} \int_{f_{\text{ring}}}^{f_{\text{cut}}} \frac{df}{S(f)} \frac{1}{f_{\text{ring}}^{4/3} f_{\text{merg}}} \times \left[1 + \left(\frac{f - f_{\text{ring}}}{\sigma/2} \right)^2 \right]^{-2},
\end{aligned} \tag{3.10}$$

where f_{merg} , f_{ring} , f_{cut} and σ are phenomenological waveform parameters [122] and f_{isco} is the redshifted frequency at the innermost circular stable orbit:

$$f_{\text{isco}} \simeq \frac{2198}{1+z} \left(\frac{M_{\text{bin}}}{M_{\odot}} \right)^{-1} \text{ Hz}. \tag{3.11}$$

Finally, the energy spectrum emitted by the binary is taken as [78, 122]:

$$\frac{dE}{df} \simeq \frac{(\pi G)^{2/3} \mathcal{M}_c^{5/3}}{3} \times \begin{cases} f^{-1/3} & f < f_{\text{merg}} \\ f_{\text{merg}}^{-1} f^{2/3} & f_{\text{merg}} \leq f < f_{\text{ring}} \\ \frac{f_{\text{merg}}^{-1} f_{\text{ring}}^{-4/3} f^2}{\left[1 + \left(\frac{f - f_{\text{ring}}}{\sigma/2} \right)^2 \right]^2} & f_{\text{ring}} < f \leq f_{\text{cut}} \end{cases}. \tag{3.12}$$

3.2 SGWB anisotropies

Similarly to the isotropic term $\bar{\Omega}_{\text{gw}}(f_o)$, also $\delta\Omega_{\text{gw}}(f_o, \hat{e}_o)$ depends on the local astrophysics at galactic and sub-galactic scales and on the underlying cosmology. However, the anisotropies depend also on the Large Scale Structure (LSS) and its effect on the distribution of sources and on the propagation of GW. Analytic expressions for the anisotropies of the astrophysical SGWB, computed starting from the ingredients listed above, already exist in literature (see e.g. [84, 90, 95, 96]).

Since the anisotropies in the total matter density are encoded in the anisotropic component of the SGWB, the latter can be considered a tracer of the former. This argument allows us to exploit the public code CLASS [100, 101], without the necessity of modifying it, for computing the angular power spectrum of the SGWB anisotropies. Indeed, the formalism for the computation of the SGWB anisotropy power spectrum is similar to the one used for computing the power spectrum of galaxy number counts. We can therefore use the CLASS routines dedicated to number counts [123] also in our case. Despite the analogy in the two formalisms, there are indeed deep conceptual differences that have to be dealt with carefully. In fact, the physics of number counts is intrinsically tomographic, whereas the physics of SGWB is somehow blind to the location in redshift space of the sources, since the superposition of all the unresolved events is calculated integrating along z . Therefore, in order to adapt

the number count formalism to the SGWB, we must reduce the analysis to a single redshift bin that spans from $z = 0$ up to a certain z_{max} , beyond which the GW contributions are negligible. In this way, all the events in the considered redshift range are integrated together and contribute to the angular power spectrum of the energy overdensity:

$$C_\ell = \frac{2}{\pi} \int \frac{dk}{k} P(k) \left[4\pi \frac{\delta\Omega_\ell(k)}{\Omega_{\text{gw}}} \right]^2, \quad (3.13)$$

where

$$\delta\Omega_\ell(k) = \int_0^{z_{max}} dz \frac{d\Omega}{dz} W(z, z_{max}/2) \delta\Omega_\ell(k, z). \quad (3.14)$$

In the previous expressions, $P(k)$ is the primordial matter power spectrum, $d\Omega/dz$ is the density per redshift interval of the tracer, $W(z, z_i)$ is a window function centred in $z_{max}/2$, which in our case will be a top hat in order to weight all the events equally, and $\delta\Omega_\ell(k, z)$ is the relativistic angular fluctuation of the density of the tracer, which is determined by density (den), velocity (vel), lensing (len) and gravity (gr) effects [98, 124, 125]:

$$\delta\Omega_\ell(k, z) = \delta\Omega_\ell^{\text{den}}(k, z) + \delta\Omega_\ell^{\text{vel}}(k, z) + \delta\Omega_\ell^{\text{len}}(k, z) + \delta\Omega_\ell^{\text{gr}}(k, z). \quad (3.15)$$

The relative importance between each of these terms depends on the specific configuration (redshift bins, window functions, etc.) but the main contribution is usually given by the density term. The full expressions of the relativistic effects in the fluctuation $\delta\Omega_\ell$ are:

$$\begin{aligned} \delta\Omega_\ell^{\text{den}}(k, z) &= b \delta(k, \tau_z) j_\ell \\ \delta\Omega_\ell^{\text{vel}}(k, z) &= \frac{k}{\mathcal{H}} j_\ell'' V(k, \tau_z) + \left[(f^{\text{evo}} - 3) \frac{\mathcal{H}}{k} j_\ell + \left(\frac{\mathcal{H}'}{\mathcal{H}^2} + \frac{2 - 5s}{r(z)\mathcal{H}} + 5s - f^{\text{evo}} \right) j_\ell' \right] V(k, \tau_z), \\ \delta\Omega_\ell^{\text{len}}(k, z) &= \ell(\ell + 1) \frac{2 - 5s}{2} \int_0^{r(z)} dr \frac{r(z) - r}{r(z)r} [\Phi(k, \tau_z) + \Psi(k, \tau_z)] j_\ell(kr), \\ \delta\Omega_\ell^{\text{gr}}(k, z) &= \left[\left(\frac{\mathcal{H}'}{\mathcal{H}^2} + \frac{2 - 5s}{r(z)\mathcal{H}} + 5s - f^{\text{evo}} + 1 \right) \Psi(k, \tau_z) + (5s - 2)\Phi(k, \tau_z) + \mathcal{H}^{-1}\Phi'(k, \tau_z) \right] j_\ell + \\ &\quad + \int_0^{r(z)} dr \frac{2 - 5s}{r(z)} [\Phi(k, \tau) + \Psi(k, \tau)] j_\ell(kr) + \\ &\quad + \int_0^{r(z)} dr \left(\frac{\mathcal{H}'}{\mathcal{H}^2} + \frac{2 - 5s}{r(z)\mathcal{H}} + 5s - f^{\text{evo}} \right) [\Phi(k, \tau) + \Psi(k, \tau)] j_\ell(kr), \end{aligned} \quad (3.16)$$

where b is the bias of the tracer, s is the magnification bias, f^{evo} is the evolution bias, r is the conformal distance on the light cone, $\tau = \tau_0 - r$ is the conformal time, $\tau_z = \tau_0 - r(z)$, j_ℓ, j_ℓ' and j_ℓ'' are the Bessel functions and their derivatives evaluated at $y = kr(z)$ if not explicitly stated, \mathcal{H} is the conformal Hubble parameter, the prime symbol stands for derivatives with respect to conformal time, δ is the density contrast in the comoving gauge, V is the peculiar velocity, Φ and Ψ are Bardeen potentials.

From previous expressions, it can be seen that there are four main ingredients that are needed to fully characterize our tracer: the *redshift distribution* $d\Omega/dz$, i.e. the source number density per redshift interval, the *bias* b , which quantifies the mismatch between the distribution of the matter and of the tracer, the *magnification bias* s , which quantifies the

change in the observed surface density of sources of tracer induced by gravitational lensing and the *evolution bias* f^{evo} , which reflects the fact that the number of elements of a tracer is not necessarily conserved in redshift due to the possible formation of new objects. All these quantities will be computed for the SGWB in Sub-section 4.2.

4 Results

In this Section, we report the most relevant results of our work. First of all, we discuss the features of the isotropic energy density of the SGWB originated by our astrophysical sources. Secondly, we present a full characterization of the energy density of the SGWB produced by coalescing binaries as a tracer of the distribution of galaxies and consequently of the total matter density. We then show our results for the power spectrum of the SGWB anisotropies. Finally, we develop a methodology for producing a full sky SGWB anisotropy map. All our analyses are performed for two different detectors: advanced LIGO/Virgo [52, 82] and Einstein Telescope [55–59].

4.1 Energy density of the astrophysical SGWB

In this Sub-section we present our results regarding the frequency spectrum $\bar{\Omega}_{\text{gw}}(f_o)$ of the total energy density of the SGWB. We compute the energy density for the three types of coalescing binaries, BH-BH, BH-NS and NS-NS, and we specify our results to the case where all the events, resolved and unresolved, are taken into account (figure 2) and to the cases where we subtract the resolved events by aLIGO/Virgo and ET respectively (figure 3). All the curves have the typical shape of the SGWB produced by the superposition of signals from coalescing binary systems: at low frequencies, the dominating contribution comes from the inspiral phase and the energy density is proportional to $f^{2/3}$. As the frequency increases, the contribution from the merger phase becomes more and more important and the power-law slows down until eventually the energy density starts to decrease. The frequency at which this drop occurs is related to the mass of the compact objects inside the binary: the lower is the chirp mass of the binary, the higher is the frequency at which the merger occurs. For this reason, the energy density of the SGWB produced by coalescing BH-BH binaries peaks at lower frequencies than the energy density of the SGWB produced by coalescing NS-NS. Finally, very high frequencies are associated to the ringdown phase and are characterized by an exponential drop. The great effect of different astrophysical prescriptions on the energy density [81, 87] makes it difficult to do an accurate comparison with previous results. However, we can say that both shape and amplitude of our detector-independent spectra in figure 2 are compatible with the results presented in e.g. [75–77, 87].

The ratio of the amplitudes of the backgrounds coming from different types of coalescing binaries depends on the merger rates, on the typical strength of the signals and on the number of events resolved by the detector. For our astrophysical prescriptions, NS-NS binary systems have the largest merger rate density, followed in order by BH-BH and BH-NS. On the other hand, binary systems with higher chirp mass produce a louder GW signal, so that BH-BH events are the most intense, followed by BH-NS and NS-NS. Without considering the effect of the detector, these two effects combine together such that the BH-BH systems produce the SGWB with the greatest amplitude, followed by NS-NS and BH-NS. For aLIGO/Virgo this order is preserved since the number of resolved events is moderately low. The situation is quite different for ET, which is expected to detect most of the BH-BH systems up to $z \sim 2$ and most of the NS-NS systems up to $z \sim 1$, as we will discuss in more detail in the next

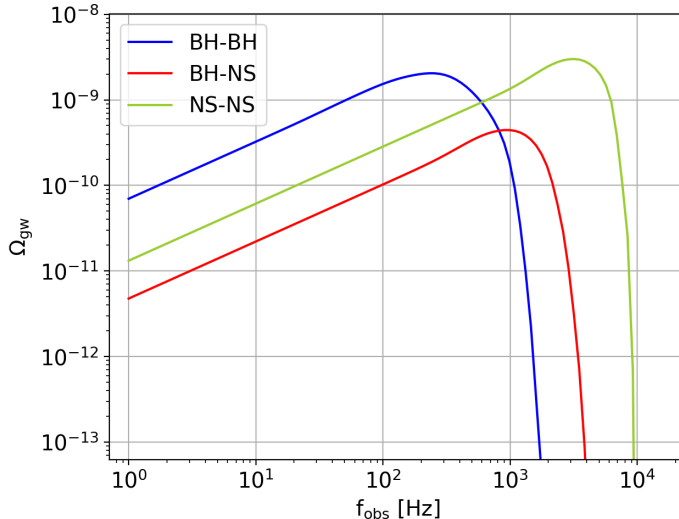


Figure 2: Energy density parameter of the SGWB constituted by all the events, resolved and unresolved, as a function of the observed frequency. The curves have been evaluated within the astrophysical set-up described in section 2, using equation (3.4) with $\bar{\rho} = \infty$: in this way the integral is equal to 1 and all the events are included in the computation of the background. Different colors are associated to the SGWB produced different type of merging binaries: BH-BH (blue), BH-NS (red) and NS-NS (green).

Sub-section. Accordingly, for ET the background produced by BH-BH events is slightly lower than the one produced by NS-NS ones. The higher sensitivity of ET is also responsible of the fact that the energy density is lower for ET than for aLIGO/Virgo: since ET will resolve a larger number of events, there will be less unresolved events to produce the SGWB.

4.2 Characterizing the SGWB as a tracer of matter

As we stressed already, in the present work we deal with the SGWB given by the superposition of the GW signals produced by merging binaries. Indeed, these GW signals originate in galaxies and therefore trace their distribution. Since galaxies trace the total matter distribution, the energy density of the SGWB itself is a tracer of matter. In this Sub-section, we characterize the astrophysical SGWB as a tracer of the total matter density in order to be able to compute the power spectrum of the anisotropies with CLASS. As already pointed out in Section 3, the four physical quantities that characterize a tracer are: redshift distribution, bias, magnification bias and evolution bias. In the following, we compute all those quantities for the energy density of the SGWB.

By definition, we can express the isotropic part of the energy density as:

$$\bar{\Omega}_{\text{gw}} \equiv \int dz \frac{d\bar{\Omega}_{\text{gw}}}{dz}. \quad (4.1)$$

By comparing the previous expression with equation (3.4), we deduce that the redshift dis-

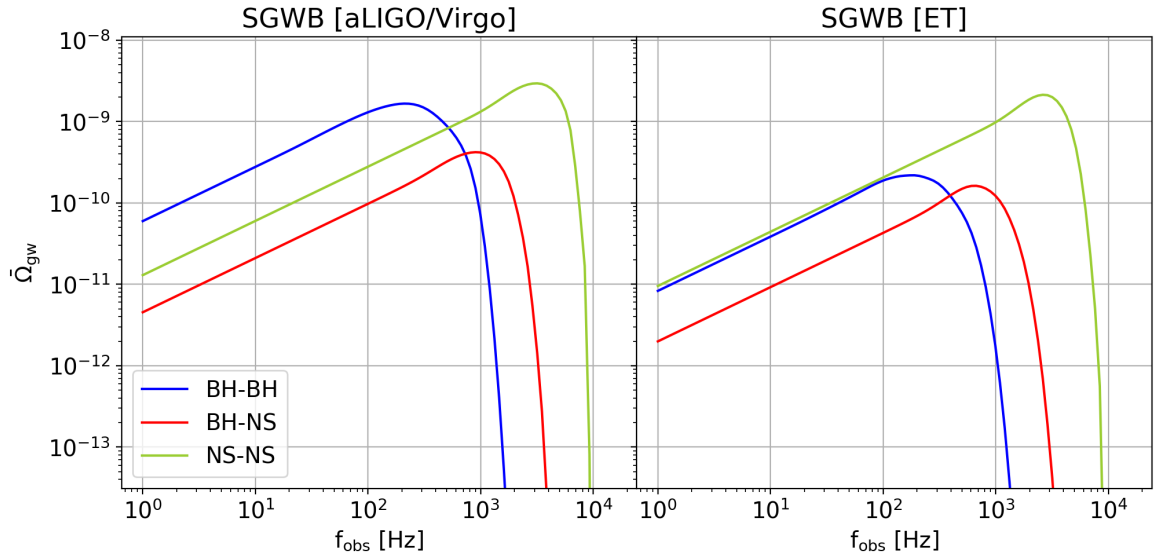


Figure 3: Energy density parameter of the SGWB as a function of the observed frequency for aLIGO/Virgo (left panel) and ET (right panel) computed using equation (3.4) within the astrophysical set-up described in section 2, using $\bar{\rho} = 8$. The color code is the same as in figure 2.

tribution of $\bar{\Omega}_{\text{gw}}$ is given by:

$$\begin{aligned} \frac{d\bar{\Omega}_{\text{gw}}}{dz}(z, f_{\text{obs}}) &= \frac{8\pi G f_{\text{obs}}}{3H_0^3 c^2} \frac{1}{(1+z) h(z)} \int d\mathcal{M}_c \frac{d^2 \dot{N}}{d\mathcal{M}_c dV}(\mathcal{M}_c, z) \frac{dE}{df}(f|\mathcal{M}_c) \times \\ &\times \int_0^{\bar{\rho}} d\rho P_\rho(\rho|\mathcal{M}_c, z). \end{aligned} \quad (4.2)$$

In figure 4 we plot $d\bar{\Omega}_{\text{gw}}/dz$ as a function of redshift at a fixed frequency of 65 Hz. We show both the contributions to the SGWB from all the merging events ($\bar{\rho} = \infty$ in the previous equation) and subtracting the resolved events by aLIGO/Virgo and ET respectively. The distribution $d\bar{\Omega}_{\text{gw}}/dz$ for all the events is almost flat up to $z \lesssim 1$ due to a compensation between the increasing number of mergers and the dilution of the GW flux, it start decreasing at $1 < z < 2$ since merging rates flatten at such redshifts, not compensating anymore for flux dilution, and then decreases rapidly due to the increasing rarity of merging binaries at high redshifts. The curves for aLIGO/Virgo and ET, on the other hand, reflect the fact that GW detectors resolve many of the nearby events (especially the brighter BH-BH ones), which hence do not contribute to the background. For this reason, the redshift distributions for aLIGO/Virgo and ET decrease also at low redshifts, so that intermediate redshift events contribute the most to the energy density of the SGWB. This effect is more important for ET, which has a higher sensitivity than aLIGO/Virgo and is expected to resolve the majority of BH-BH events up to $z \lesssim 2$ and many NS-NS events up to $z \lesssim 1$. Consequently, the bulk of the energy density will come from events located at $z \sim 1 - 2$ for ET.

The bias b_Ω for the energy density of the SGWB is directly related to the galaxy bias. In particular, since the mergers take place in all galaxy types with different rates, the correct estimate of b_Ω needs to take into account how the different galaxies are contributing to the detected signal. This is done giving proportioned weight to the bias of the host galaxies,

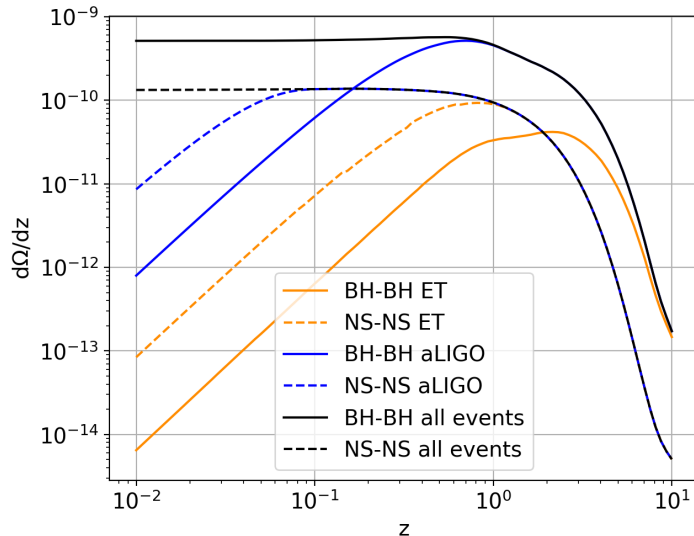


Figure 4: Distributions $d\bar{\Omega}_{\text{gw}}/dz$ for BH-BH (solid) and NS-NS (dashed) merging events at a fixed frequency of 65 Hz. The black curves are obtained considering the contribution to the SGWB of all the events, whereas the blue and orange distributions are computed subtracting the contributions of the events resolved by aLIGO/Virgo and ET, respectively.

according to their star formation rate:

$$b_{\Omega}(z, f_{\text{obs}}) = \frac{\int d \log_{10} \psi \frac{d^2 \bar{\Omega}_{\text{gw}}}{dz d \log_{10} \psi}(z, \psi, f_{\text{obs}}) b(z, \psi)}{\int d \log_{10} \psi \frac{d^2 \bar{\Omega}_{\text{gw}}}{dz d \log_{10} \psi}(z, \psi, f_{\text{obs}})}. \quad (4.3)$$

In the previous equation, the energy density per unit redshift and SFR is obtained from the merger rate per unit volume, chirp mass and SFR in the following way:

$$\begin{aligned} \frac{d\bar{\Omega}_{\text{gw}}}{dz d \log_{10} \psi}(z, f_{\text{obs}}) &= \frac{8\pi G f_{\text{obs}}}{3H_0^3 c^2} \frac{1}{(1+z) h(z)} \int d\mathcal{M}_c \frac{d^2 \dot{N}}{d\mathcal{M}_c dV d \log_{10} \psi}(\mathcal{M}_c, z) \times \\ &\times \frac{dE}{df}(f|\mathcal{M}_c) \int_0^{\bar{\rho}} d\rho P_{\rho}(\rho|\mathcal{M}_c, z). \end{aligned} \quad (4.4)$$

The quantity $b(z, \psi)$, on the other hand, is the galaxy bias as a function of redshift and SFR. Following the procedure depicted in [126], we associate the SFR of each galaxy to the mass of the hosting dark matter halo through an abundance matching technique and then we assign to a galaxy with given SFR the bias of the corresponding halo. The abundance matching is a standard method to derive a monotonic relationship between the galaxy and the halo properties by matching the corresponding number densities in the following way:

$$\int_{\log_{10} \psi}^{\infty} d \log_{10} \psi' \frac{dN}{d \log_{10} \psi' dV} = \int_{-\infty}^{\infty} d \log_{10} M'_H \frac{dN}{d \log_{10} M'_H dV} \frac{1}{2} \text{erfc} \left[\frac{\log_{10}(M_H(\psi))/M'_H}{\sqrt{2}\tilde{\sigma}} \right], \quad (4.5)$$

where $dN/d \log_{10} \psi'/dV$ is the star formation rate function and $dN/d \log_{10} M'_H/dV$ is the galaxy halo mass function, i.e. the mass function of halos that are hosting one individual

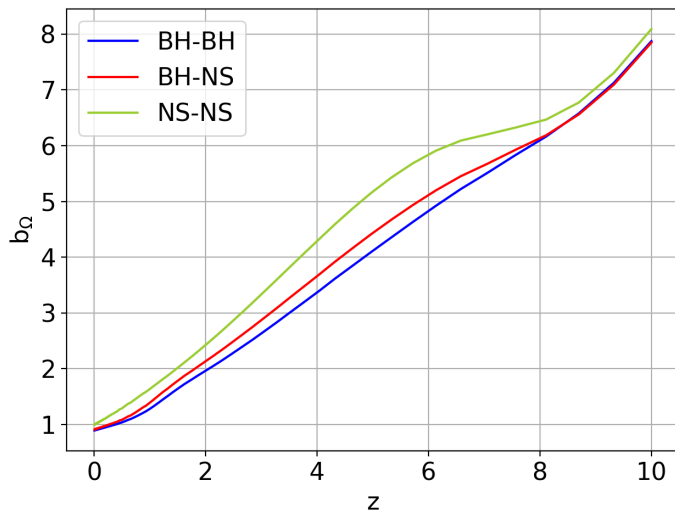


Figure 5: SGWB energy density bias for the three types of DCO mergers (BH-BH, BH-NS and NS-NS) as a function of redshift at 65 Hz for ET. For all the types of merger the bias is a strongly increasing function of redshift.

galaxy (see Appendix A of [126] for further details). $M_H(\psi)$ is the relation we are looking for and $\tilde{\sigma} \equiv \sigma d \log_{10} M_H / d \log_{10} \psi$ is the scatter around that relation (we set $\sigma_{\log_{10} \psi} \simeq 0.15$). Once $M(\psi)$ is determined, we assign to each galaxy the bias corresponding to the halo associated with its SFR, i.e $b(z, \psi) = b(z, M_H(z, \psi))$, where $b(z, M_H)$ is computed as in [127] and approximated as in [128]. Finally, once $b(z, M_H(z, \psi))$ has been obtained, we can compute the bias for the SGWB energy density according to Equation (4.3). As an example, in figure 5 we show the SGWB bias for the three types of DCO mergers (BH-BH, BH-NS and NS-NS) as a function of redshift at 65 Hz for the ET.

Let’s now move to the analysis of lensing effects on the SGWB. For what concerns weak lensing, two effects compete against each other: on one side, the energy density is increased because some of the unresolved events that make up the signal are boosted by the lensing; on the other side, the associated dilution of the volume reduces the received GW flux. Adapting the definition of the magnification bias for resolved GW events from [98, 129, 130] to the SGWB, we get:

$$s_{\Omega, \bar{\rho}}(z, f_{\text{obs}}) = \left. \frac{d \log_{10} \left(\frac{d \bar{\Omega}_{\text{gw}}(f_{\text{obs}}, z, < \rho)}{dz} \right)}{d \log_{10} \rho} \right|_{\rho = \bar{\rho}}. \quad (4.6)$$

The sign difference with respect to [98, 130] is due to the fact that we are now considering all the GW events that are below the detection threshold $\bar{\rho}$. As already shown in [95], however, weak lensing does not affect the anisotropies of the SGWB at first order, meaning that the two effects described before cancel out. For this reason, we set the magnification bias to 0.4, i.e. the value for which the two competing effects balance each other. Nonetheless, this compensation is not necessarily true for strong lensing: in fact, in the latter case some events are “kicked” beyond the detection threshold $\bar{\rho}$ by lensing magnification, causing a reduction of the unresolved events constituting the SGWB: $\bar{\Omega}_{\text{gw, lensed}} = \bar{\Omega}_{\text{gw}} - \bar{\Omega}_{\text{gw, kicked}}$. The effect of a gravitational lens with magnification μ on a GW event with signal to noise ρ is to enhance the signal to noise of a factor $\sqrt{\mu}$, without changing the observed waveform (due to the

achromaticity of lensing in the geometrical-optics limit). The reduction of the SGWB caused by the lensing “kicking” some events beyond the detection threshold can be computed as:

$$\begin{aligned} \bar{\Omega}_{\text{gw,kicked}} &= \frac{8\pi G f_{\text{obs}}}{3H_0^3 c^2} \int dz \int d\mathcal{M}_c \frac{R_{\text{merge}}(\mathcal{M}_c, z)}{(1+z) h(z)} \frac{dE}{df}(f|\mathcal{M}_c) \times \\ &\times \int_0^{\bar{\rho}} d\rho P_\rho(\rho|\mathcal{M}_c, z) \int_{\bar{\mu}(\rho)}^\infty \frac{dp}{d\mu} d\mu, \end{aligned} \quad (4.7)$$

where $dp/d\mu$ is the magnification probability distribution from [131], which depends on the redshift of the GW source and on the properties of the intervening galaxies acting as lenses, and $\bar{\mu}(\rho) = \min[2, (8/\rho)^2]$ ³. We verified that this correction turns out to be negligible, being more than 4 orders of magnitude fainter than $\bar{\Omega}_{\text{gw}}$.

Finally, the evolution bias for the SGWB can be written as:

$$f_\Omega^{\text{evo}} = \frac{d \ln \left(\frac{d\bar{\Omega}_{\text{gw}}}{dz d\omega} \right)}{d \ln a}, \quad (4.8)$$

where a is the scale factor and ω is the solid angle. The evolution bias appears only in sub-leading contributions, since it is just present in the non-dominant part of the velocity term and in the gravity term of equation (3.15).

4.3 Angular power spectrum of SGWB anisotropies

We compute the angular power spectrum of the SGWB anisotropies for a single redshift bin, $0 < z < 8$, using a tophat window function, in order to weight all the events equally. We exploit the CLASS public code, which allows to insert only one value of bias and magnification bias per redshift bin. This is not a problem for the magnification bias because, as we saw, lensing does not contribute to the anisotropies at first order, so that $s = 0.4$ at every z . However, this feature is indeed a limitation for what concerns the bias, which increases consistently with redshift, as can be seen in figure 5. To overcome this problem, we weighted the bias over the redshift distribution of the energy density:

$$\langle b_\Omega \rangle = \frac{\int dz \frac{d\bar{\Omega}_{\text{gw}}}{dz} b_\Omega}{\int dz \frac{d\bar{\Omega}_{\text{gw}}}{dz}}. \quad (4.9)$$

Of course, given the strong redshift dependence of the bias, this is an approximation that should be improved in the future by modifying the CLASS code in order to obtain more precise results. Nevertheless, we notice that the discrepancy should not be very large, since the events that are characterized by a very high value of the bias are very rare, while the ones that have a sensibly lower bias are located at low redshift and hence are probably resolved, so that they do not contribute to the SGWB.

The angular power spectra of the SGWB anisotropies at a reference frequency for ET and aLIGO/Virgo are shown in figure 6. For both detectors and for all types of events, the power spectrum behaves like a power law at large scales and then bends at smaller scales. For ET the power law slope is roughly constant among the different type of sources and it is close to the slope of the power spectrum for point like sources ($\propto \ell^2$) plus a certain distortion.

³We consider $\mu = 2$ the value of magnification that discriminates between weak and strong lensing.

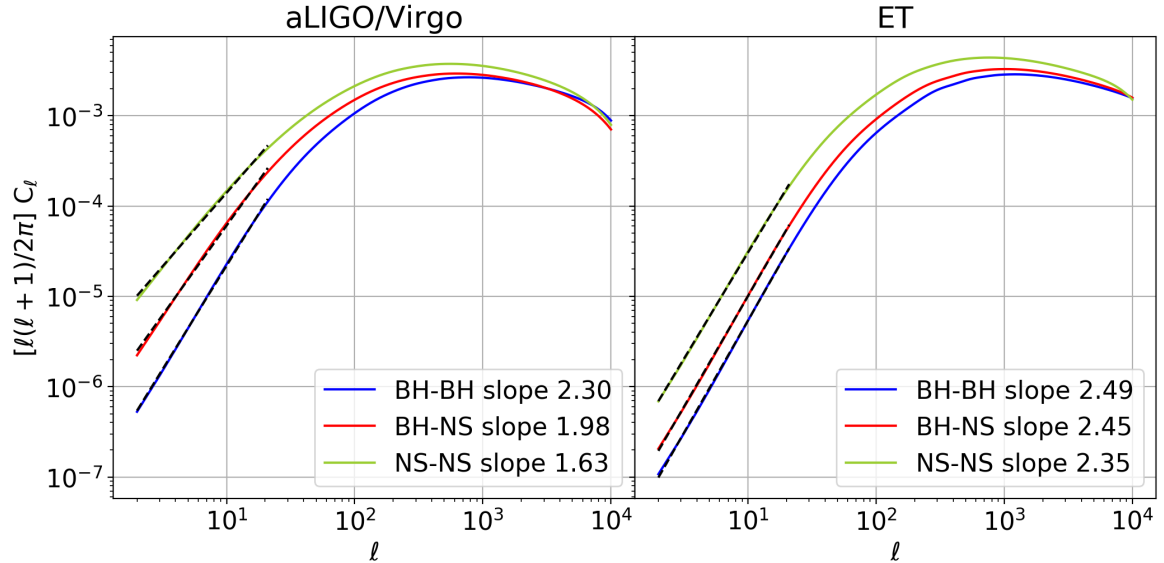


Figure 6: Angular power spectra of the SGWB anisotropies for aLIGO/Virgo (left) and ET (right) for BH-BH, BH-NS and NS-NS events at a fixed frequency of 65 Hz. The black dotted lines represent the power-law fit at large scales, whose slopes are also reported.

For aLIGO/Virgo, on the contrary, the slopes are different depending on the type of source. In particular, BH-BH events have the steepest slope, while NS-NS events have the mildest one. We investigated the frequency behaviour of the curves producing power spectra for $f = 33, 65, 105$ and 209 Hz. Interestingly, we found that the large scale slopes are constant with frequency: this is a very useful feature that could be used to distinguish the contribution of the various type of coalescing binaries from possible future measurements.

Finally, in order to obtain a detector-independent result to be compared with literature, we computed the power spectrum of the SGWB anisotropies constituted by the superposition of all GW events, resolved and unresolved. As we can see in figure 7, also in this case the power spectra behave as a power-law on large scales and bends at smaller scales. This time, however, the slope of the power-law is close to 1, which means that $C_\ell \propto 1/\ell$. Despite the differences in the astrophysical prescriptions and in the approach to the power spectrum computation, our results are in rather good agreement with the ones presented in [86, 87]. Consider e.g. the ‘linear’ curve at 32 Hz in figure 2 of reference [86]: the position of the peak and the associated value of the power spectrum are compatible with our results at 65 Hz within a factor 2. On the other hand, we find a discrepancy with the results obtained from the Millennium simulation presented in [91–93]. Our power spectra, previously re-scaled for the average energy density $\bar{\Omega}_{\text{gw}}/4\pi$, are at least one order of magnitude lower than the ones presented in the left panel in figure 1 of reference [93].

The interpretation of the features of these power spectra is not trivial. The SGWB is given by the superposition of all the unresolved GW events up to a typical maximum redshift z_{max} , which is the maximum redshift at which sources can be observed by a given detector at a given frequency. It follows that there is no direct relation between wave modes and an angular scales. For a fixed observed frequency, in fact, a given wave-mode contributes to all multipoles such that $\ell \lesssim \ell_{\text{max}}(k)$, where $\ell_{\text{max}}(k)$ is related to z_{max} by

$$\ell_{\text{max}}(k) = k[\eta_0 - \eta(z_{\text{max}})], \quad (4.10)$$

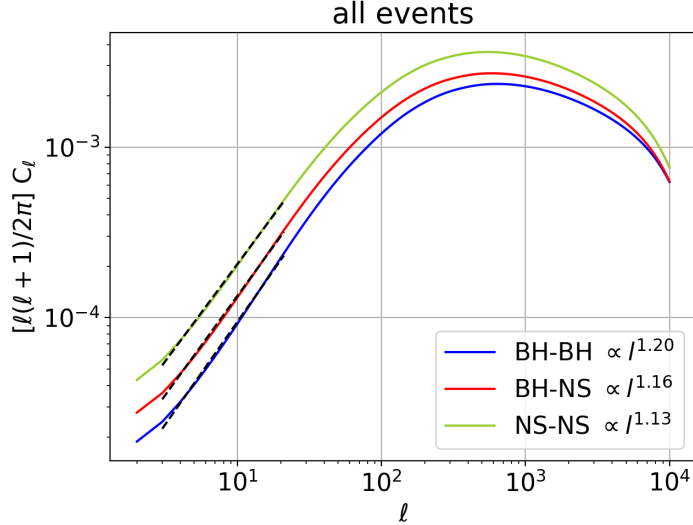


Figure 7: Angular power spectra of the SGWB anisotropies obtained integrating the signals of all the events, resolved and unresolved, at 65 Hz. The behaviour of the curves is a power-law on large scales that bends and starts to decrease at smaller scales. The slope of the power-law is ~ 1 for all types of binaries. This plot is easily compared and in good agreement with other results already present in literature [86, 87, 93].

where $\eta(z)$ is the conformal time and $\eta_0 = \eta(0)$. Nevertheless, it is possible to identify the contributions from events coming from different redshift ranges performing a sort of “tomographic” analysis that has to be interpreted in the light of the redshift distribution of the energy density $d\bar{\Omega}_{\text{gw}}/dz$. As a first step, we consider a constant redshift distribution $d\Omega/dz = 1$, in order to isolate the contributions of objects located at different redshifts. In Figure 8, we show the auto-correlations in the redshift bins $z \in [0, 1]$, $[1, 3]$ and $[3, 8]$. We focus on the shape of the curves and do not consider their amplitude, which is typically higher for thinner redshift bins due to the normalization of the window functions and is not relevant for our current purposes. Observing how the shape at large angular scales varies changing the redshift bin, we deduce that the slope of the power-law is steeper when we take into account events coming from higher redshifts (i.e. $z \in [1, 3]$ and $[3, 8]$). On the other hand, observing the behaviour at small scales, we deduce that the bending of the power spectrum is more pronounced when we consider events coming from lower redshifts (i.e. $z \in [0, 1]$ and $[0, 8]$, where all nearby events are taken into account). This is due to the fact that, at a given scale, an event coming from a certain redshift can contribute only up to a maximum multipole given by $\ell_{\text{max}}(z, k) = k[\eta_0 - \eta(z)]$: consequently, the contribution of low redshift events drops at very small angular scales.

Let’s now consider the real redshift distributions of figure 4 and perform the same tomographic analysis described above. Panels 9a and 9b show the results for the SGWB obtained from the superposition of all the events. In this case, the redshift distribution is flat up to $z \sim 1 - 2$: since the strongest contributions surely come from the most nearby objects, it is not surprising that the situation is quite similar to the one of the uniform $d\Omega/dz$. Panels 9c and 9d, on the other hand, show the results for aLIGO/Virgo. In this case, the results for two types of sources are quite different and reflect the fact that most of the nearby BH-BH mergers are resolved by aLIGO/Virgo, whereas many of the nearby NS-NS mergers are not.

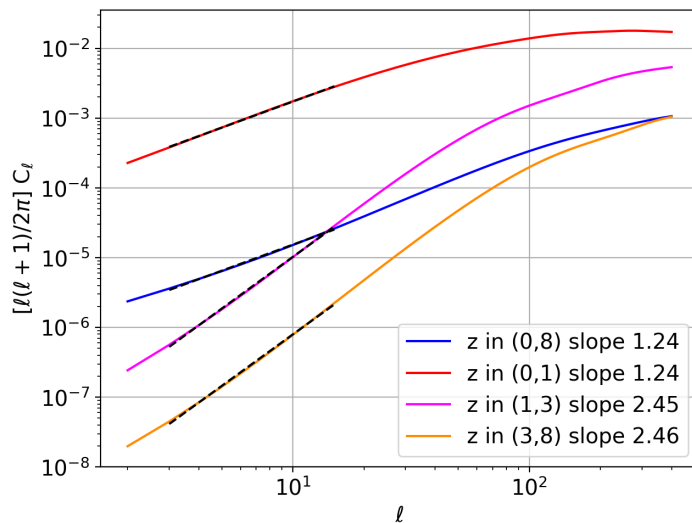


Figure 8: “Tomographic” analysis for a constant redshift distribution in order to isolate the contribution of near/distant sources. The different curves are the auto-correlations in the redshift bins $z \in [0, 1]$, $[1, 3]$ and $[3, 8]$ and in the total redshift interval $z \in [0, 8]$. As explained in the text, the slope and the curvature of the power spectrum are related to the redshift location of the sources.

Accordingly, in the NS-NS case there are quite a lot of low redshift events that contribute to the power spectrum, so that the auto-correlation in the first redshift bin displays a milder slope and a softer bending with respect to second and the third ones. This is also the reason why the auto-correlation in the entire redshift bin $z \in [0, 8]$ for the NS-NS case has a shallower power-law behaviour at large scales with respect to the BH-BH case. Finally, as we can see in panels 9c and 9f, the higher sensitivity of ET will allow to resolve almost all the nearby NS-NS too, so that there is no substantial difference in the power spectrum behaviour for the two types of sources.

4.4 SGWB anisotropy sky map

In this Sub-section, we exploit a map-making methodology in order to complement the power spectrum analysis above with realizations of the full sky anisotropy maps corresponding to the SGWB overdensity δ_{gw} . The peculiarity of the astrophysical SGWB with respect to other backgrounds, such as the Cosmic Microwave Background (CMB), is that it originates from unresolved point sources and hence its statistics follows a Poisson distribution instead of a Gaussian one. We therefore need to produce a map of the anisotropies following a Poisson statistic with the cosmological clustering expected for the emitters that we obtained in the previous Sub-section. For this purpose, we adapt the procedure depicted in [132] to the case of the SGWB.

A preliminary step is to produce a Poisson map of the energy overdensity without any clustering. First of all, we compute the mean number of unresolved events per unit time ⁴ in

⁴In our case, we count the events occurring in one year: this is tantamount to integrating the signal over $T = 1$ yr. The choice of the integration time determines the mean number of events per pixel and hence the amplitude of the poissonian noise, as we will see in the following. See [89, 93, 94] for a detailed treatment of shot noise.

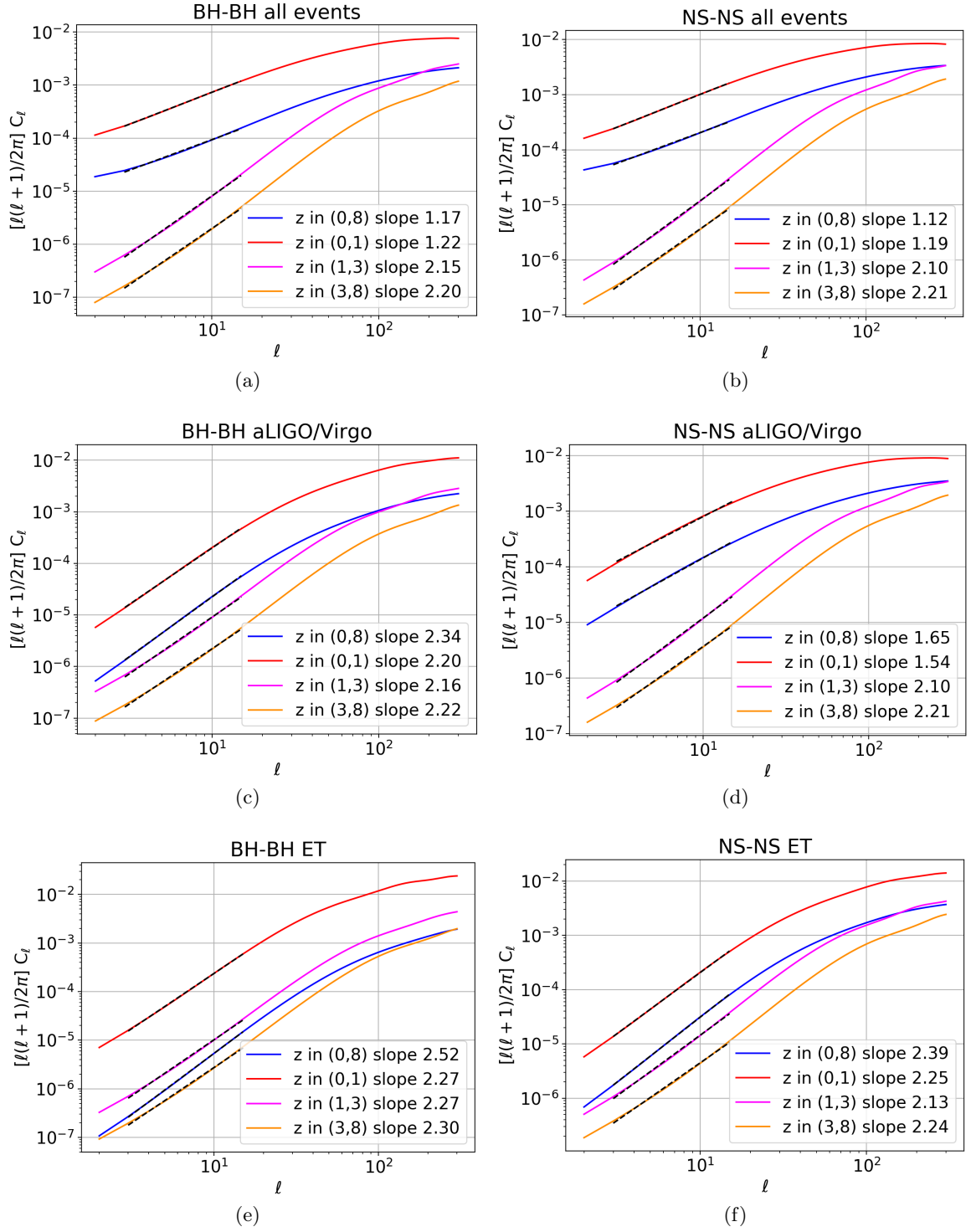


Figure 9: “Tomographic” analysis applied to the anisotropies of the SGWB generated from BH-BH and NS-NS coalescing binaries considering all events (upper panels), for aLIGO/Virgo (middle panels) and for ET (lower panels) at 65 Hz. As explained in the text, the large scale slope and the small scale bending of the power spectra allow to isolate the contributions of near and distant sources.

each pixel:

$$\langle \dot{N}_{\text{pix}} \rangle = \frac{4\pi}{N_{\text{pix}}} \int dz \int d\mathcal{M}_c \frac{d\dot{N}}{d\omega dz d\mathcal{M}_c} \int_0^{\bar{\rho}} d\rho P_\rho(\rho|z, \mathcal{M}_c). \quad (4.11)$$

In the previous expression, N_{pix} is the number of pixels in the map and $d\dot{N}/d\omega dz d\mathcal{M}_c$ is the merger rate per unit redshift, solid angle and chirp mass, which can be easily obtained from the differential merger rate of equation (2.1) through:

$$\frac{d\dot{N}}{d\omega dz d\mathcal{M}_c} = \frac{d\dot{N}}{dV d\mathcal{M}_c} \frac{c r(z)}{H_0 h(z)}, \quad (4.12)$$

where $r(z)$ is the comoving distance. We then create a map assigning to each pixel a number of events per unit time extracted from a Poisson distribution with mean $\langle \dot{N}_{\text{pix}} \rangle$. We assign to each event in each pixel a chirp mass and a redshift that we generate randomly from a 2D probability distribution obtained from the differential merger rate $d\dot{N}/dz d\mathcal{M}_c$. In this way, we can compute the energy density in each pixel summing the contributions from all the events:

$$\Omega_{\text{gw}}^{\text{Pois}} = \frac{8\pi G f_o}{3H_0^2 c^3} \frac{1}{T} \sum_i \frac{\frac{dE}{df}(z_i, \mathcal{M}_{ci})}{4\pi(1+z_i)r^2(z)}, \quad (4.13)$$

where T is the considered unit of time ($T = 1$ yr in our case). At this stage, we have a map of the SGWB energy density which follows a pure Poisson statistics, without any clustering. In order to take the latter into account, first of all we compute the Poisson map of the density contrast:

$$\delta_{\text{gw}}^{\text{Pois}} = \frac{\Omega_{\text{gw}}^{\text{Pois}} - \langle \Omega_{\text{gw}} \rangle}{\langle \Omega_{\text{gw}} \rangle}. \quad (4.14)$$

Using the HEALPix⁵ package [133, 134], we compute its harmonic coefficients $a_{\ell m}^{\text{Pois}}$. Subsequently, we introduce the correlation given by the angular power spectrum C_ℓ^{cl} obtained with CLASS in the following way:

$$a_{\ell m}^{\text{cl}} = a_{\ell m}^{\text{Pois}} \frac{\sqrt{C_\ell^{\text{Pois}} + C_\ell^{\text{cl}}}}{\sqrt{C_\ell^{\text{Pois}}}}. \quad (4.15)$$

Finally, by performing an inverse harmonic transform, we obtain the clustered Poisson density contrast $\delta_{\text{gw}}^{\text{cl}}$, from which the energy density at each pixel can be easily computed as $\Omega_{\text{gw}}^{\text{cl}} = \langle \Omega_{\text{gw}} \rangle (1 + \delta_{\text{gw}}^{\text{cl}})$. In Figure 10, we show a full sky realization of the density contrast of the GW backgrounds produced by BH-BH and NS-NS mergers at 65 Hz for ET. In Figure 11, we plot the power spectra of the two maps, together with the theoretical power spectra obtained with CLASS and the power spectra of the pure poissonian maps (no clustering). As expected, the Poisson noise power spectrum is proportional to ℓ^2 and its amplitude is related to the chosen integration time (one year in our case). By increasing the integration time, the number N of events taken into account in each pixel would increase and the noise amplitude would decrease as $1/\sqrt{N}$. We find that for $T = 1$ yr the Poisson noise dominates over the signal, especially for the BH-BH component of the SGWB. The noise is lower for the NS-NS component because the merger rate - and hence the number of events per year in each pixel - is higher for NS-NS binaries than for BH-BH ones. In both maps the intrinsic correlation of the signal is higher than the Poisson noise at very large scales ($\ell = 1$), a feature that can also be seen observing

⁵<http://healpix.sourceforge.net>

the clustering in maps. From these results it is clear that being able to remove the shot noise component is of primary importance in order to extract a measurement of the power spectrum of the SGWB from real data. Recent studies address specifically this issue [89, 93, 94]: the effect of Poisson noise can be reduced increasing the integration time or cross-correlating the signal with other probes [84, 87, 135]. A detailed analysis of the shot noise goes beyond the purposes of the present paper, but it is a crucial issue that will be surely addressed more deeply in future works.

5 Conclusions

In this paper, we studied the SGWB originated from the superposition of unresolved signals from merging compact binaries in galaxies, which is expected to be one of the dominant contributions of the total GW background in the LIGO/Virgo and ET frequency bands. The large amount of astrophysical and cosmological information encoded in this particular component of the SGWB makes its characterization one of the main goals for the GW community. Our predictions rely on an empirical approach to galactic astrophysics that allows to follow the evolution of individual systems and on the results of the population synthesis code STARTRACK to model stellar and binary evolution.

For the first time we have characterized the adimensional energy density parameter of the SGWB as a tracer of matter density, computing its redshift distribution, bias, magnification bias and evolution bias. With these elements and exploiting the similarities with the number counts formalism, we adapted the public code CLASS to the computation of the angular power spectrum of the SGWB anisotropies, taking into account lensing and relativistic corrections. We have obtained predictions concerning the isotropic energy density and the angular power spectrum of SGWB anisotropies for aLIGO/Virgo and ET. Furthermore, we also considered the case where all the events are taken into account, in order to compare with previous works in literature. All the results are diversified with respect to the various type of events (BH-BH, BH-NS and NS-NS) and the redshift location of the sources.

For what concerns the isotropic component of the SGWB, we examined in detail the spectral shape of the energy density for all types of sources, comparing the results for the two detectors. In all cases, we recovered the well known power law behaviour with spectral index $2/3$ at low frequencies with an exponential decrease at higher frequencies, depending on the typical chirp mass of the sources. In the case of the aLIGO/Virgo the dominating contribution to the energy density comes from BH-BH events, followed in order by BH-NS and NS-NS. For the ET, on the contrary, the contribution of NS-NS exceeds the one from BH-BH. This is due to the fact that ET is expected to resolve most of the low redshift BH-BH events. The better sensitivity of ET is also the reason why the overall energy of the SGWB is lower than in the aLIGO/Virgo case. In fact, for all types of mergers, the bulk of the contribution to the energy density is lower and comes from $z \sim 1 - 2$ for ET, whereas for aLIGO/Virgo is higher and more spread in redshift.

Conversely, for the case of the SGWB anisotropies power spectrum, we found a power law behaviour on large angular scales and a progressive drop at small scales, due to the lack of sources at very high redshifts. We performed a “tomographic” analysis in order to isolate the contribution of sources at different redshifts. We found that the slope of the power-law is related to nearby sources: the less they contribute, the steeper is the power spectrum. Accordingly, for the ET all the sources have the same slope ~ 2.5 , since all events at low

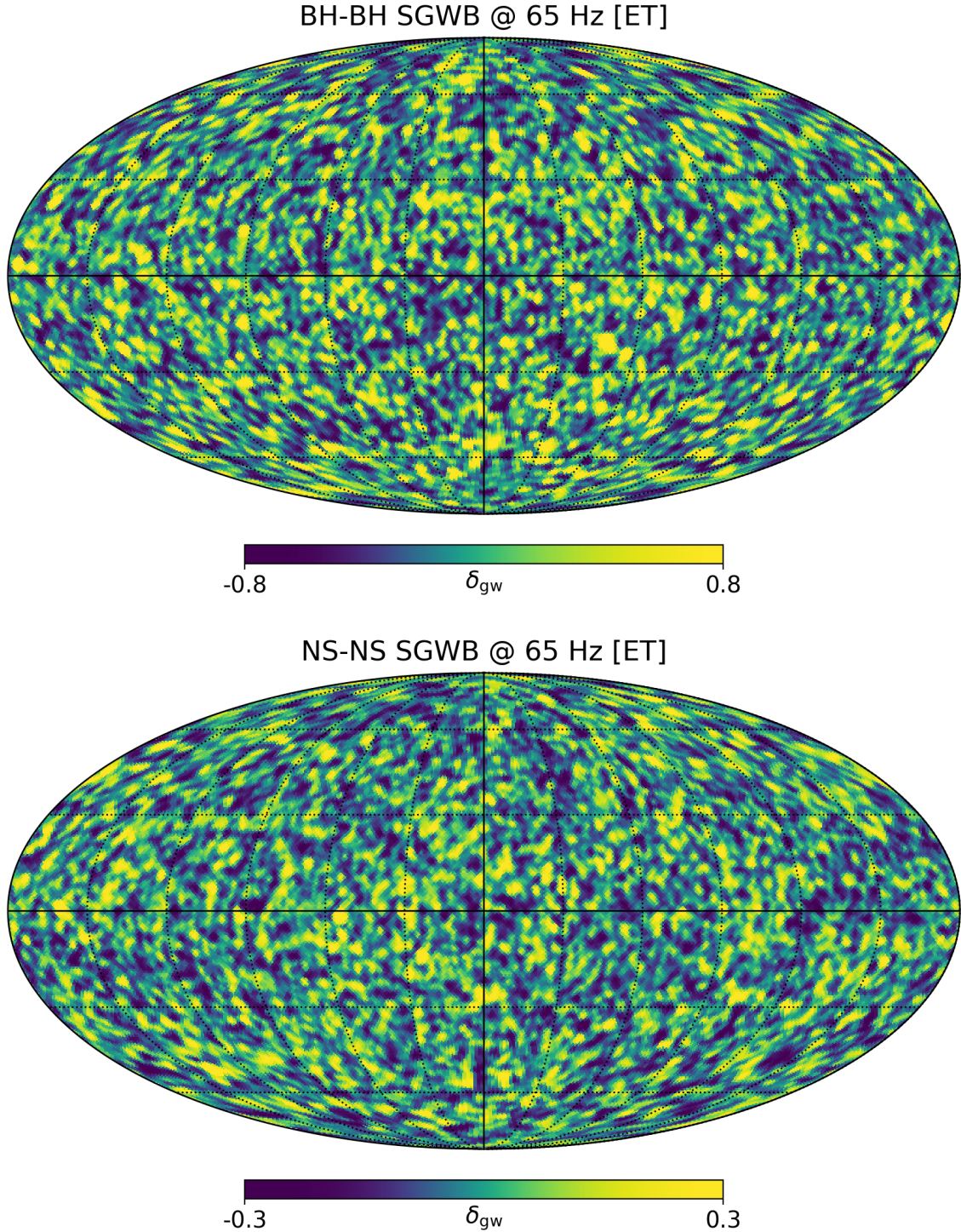


Figure 10: Mollweide maps of the energy density contrast of the SGWB produced by BH-BH (upper panel) and NS-NS (lower panel) mergers at 65 Hz for Einstein Telescope with integration time $T = 1$ yr. The plots have been realized with the HEALPix package, using $N_{\text{side}} = 64$, which corresponds to an angular resolution of $\theta_{\text{pix}} = 55'$. In order to remove the ringing effect arising when manipulating the harmonic coefficients, the maps have been smoothed with a Gaussian filter corresponding to $\sigma = \theta_{\text{pix}}$.

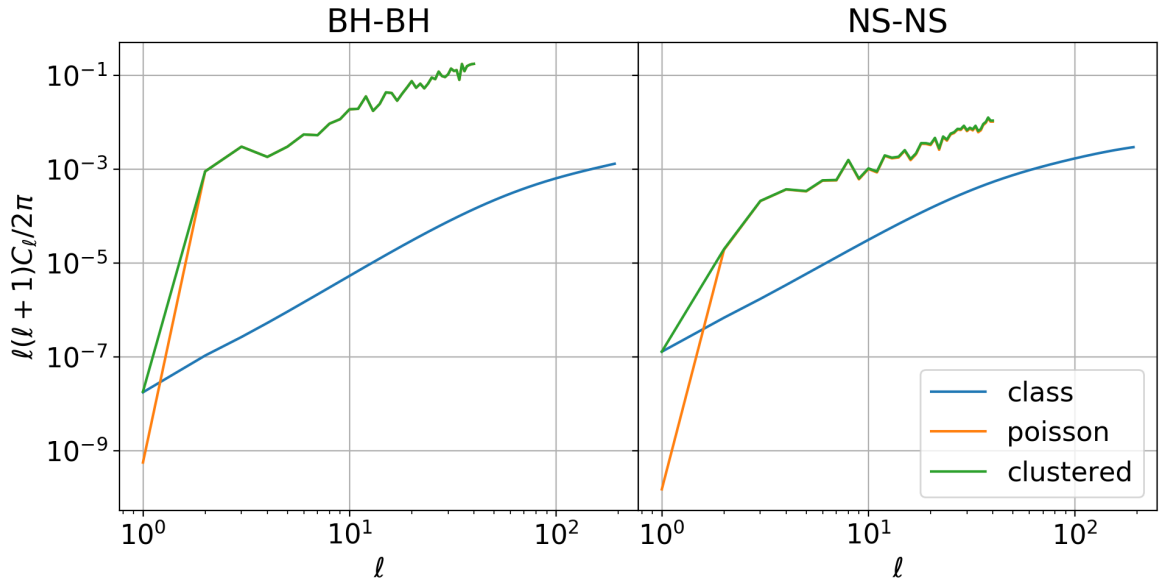


Figure 11: Comparison among the power spectrum of the simulated SGWB maps (green), the theoretical power spectrum of the SGWB anisotropies obtained with CLASS (blue) and the power spectrum of pure Poisson noise (orange). The contribution of shot noise is $\propto \ell^2$ and it dominates over the signal at most scales. As expected, the noise is lower in the NS-NS case, since the merger rate is higher than the BH-BH one.

redshift are expected to be resolved, whereas for aLIGO/Virgo the slope is steeper for BH-BH events milder for NS-NS ones.

Finally, we presented a procedure to simulate realizations of the SGWB starting from the theoretical predictions of the power spectrum obtained with CLASS, and combining the Poisson nature of the statistics with the cosmological clustering properties. With this procedure, we obtained a high-resolution full sky map of the SGWB overdensity. The Poisson noise dominates over the pure clustering signal at all the considered angular scales, especially for the SGWB generated by BH-BH events, whose merger rate is lower than NS-NS ones.

In future works, we are going to extend the results of the present paper in a twofold way. First, we will exploit our analysis and techniques to cross-correlate the SGWB with other cosmological and astrophysical probes. This will be extremely useful in order to reduce the effects of Poisson noise and of systematic uncertainties, as well as to extract richer and more robust physical information. In addition, we will investigate how different stellar and galactic prescriptions affect our results. In fact, a detailed assessment of the modeling uncertainties in the astrophysical SGWB will constitute a primary issue for the component separation of the GW background, especially in the challenging search of the primordial contribution.

Acknowledgments

A.L. acknowledges support from the PRIN MIUR 2017 prot. 20173ML3WW 002, ‘Opening the ALMA window on the cosmic evolution of gas, stars and supermassive black holes’ and the EU H2020-MSCA-ITN-2019 Project 860744 ‘BiD4BEST: Big Data applications for Black hole Evolution Studies’. G.C., G.S. and C.B. are partially supported by the INDARK INFN grant. C.B. acknowledges support from the COSMOS and LiteBIRD networks of the Italian

Space Agency (www.cosmosnet.it). The authors would like to thank Daniele Bertacca and Nicola Bellomo for useful discussions. Some of the results in this paper have been derived using the healpy and HEALPix packages [133, 134].

References

- [1] B. P. Abbott et al. Observation of Gravitational Waves from a Binary Black Hole Merger. Phys. Rev. Lett., 116(6):061102, 2016.
- [2] B. P. Abbott et al. Binary Black Hole Mergers in the first Advanced LIGO Observing Run. Phys. Rev. X, 6(4):041015, 2016. [Erratum: Phys.Rev.X 8, 039903 (2018)].
- [3] B. P. Abbott et al. GW151226: Observation of Gravitational Waves from a 22-Solar-Mass Binary Black Hole Coalescence. Phys. Rev. Lett., 116(24):241103, 2016.
- [4] Benjamin P. Abbott et al. GW170104: Observation of a 50-Solar-Mass Binary Black Hole Coalescence at Redshift 0.2. Phys. Rev. Lett., 118(22):221101, 2017. [Erratum: Phys.Rev.Lett. 121, 129901 (2018)].
- [5] B. P. Abbott et al. GW170814: A Three-Detector Observation of Gravitational Waves from a Binary Black Hole Coalescence. Phys. Rev. Lett., 119(14):141101, 2017.
- [6] B. P. Abbott et al. GW170817: Observation of Gravitational Waves from a Binary Neutron Star Inspiral. Phys. Rev. Lett., 119(16):161101, 2017.
- [7] B. . P. . Abbott et al. GW170608: Observation of a 19-solar-mass Binary Black Hole Coalescence. Astrophys. J., 851(2):L35, 2017.
- [8] B. P. Abbott et al. GWTC-1: A Gravitational-Wave Transient Catalog of Compact Binary Mergers Observed by LIGO and Virgo during the First and Second Observing Runs. Phys. Rev. X, 9(3):031040, 2019.
- [9] B. P. Abbott et al. GW190425: Observation of a Compact Binary Coalescence with Total Mass $\sim 3.4M_{\odot}$. Astrophys. J. Lett., 892(1):L3, 2020.
- [10] R. Abbott et al. GW190412: Observation of a Binary-Black-Hole Coalescence with Asymmetric Masses. Phys. Rev. D, 102(4):043015, 2020.
- [11] R. Abbott et al. GW190814: Gravitational Waves from the Coalescence of a 23 Solar Mass Black Hole with a 2.6 Solar Mass Compact Object. Astrophys. J. Lett., 896(2):L44, 2020.
- [12] R. Abbott et al. GW190521: A Binary Black Hole Merger with a Total Mass of $150M_{\odot}$. Phys. Rev. Lett., 125(10):101102, 2020.
- [13] R. Abbott et al. GWTC-2: Compact Binary Coalescences Observed by LIGO and Virgo During the First Half of the Third Observing Run. 10 2020.
- [14] Benjamin P. Abbott et al. Upper Limits on the Stochastic Gravitational-Wave Background from Advanced LIGO’s First Observing Run. Phys. Rev. Lett., 118(12):121101, 2017. [Erratum: Phys.Rev.Lett. 119, 029901 (2017)].
- [15] B.P. Abbott et al. Search for the isotropic stochastic background using data from Advanced LIGO’s second observing run. Phys. Rev. D, 100(6):061101, 2019.
- [16] R. Abbott et al. Upper Limits on the Isotropic Gravitational-Wave Background from Advanced LIGO’s and Advanced Virgo’s Third Observing Run. 1 2021.
- [17] Benjamin P. Abbott et al. Directional Limits on Persistent Gravitational Waves from Advanced LIGO’s First Observing Run. Phys. Rev. Lett., 118(12):121102, 2017.
- [18] B.P. Abbott et al. Directional limits on persistent gravitational waves using data from Advanced LIGO’s first two observing runs. Phys. Rev. D, 100(6):062001, 2019.

- [19] Nelson Christensen. Stochastic Gravitational Wave Backgrounds. Rept. Prog. Phys., 82(1):016903, 2019.
- [20] Andrew H. Jaffe and Donald C. Backer. Gravitational waves probe the coalescence rate of massive black hole binaries. Astrophys. J., 583:616–631, 2003.
- [21] Luke Zoltan Kelley, Laura Blecha, Lars Hernquist, Alberto Sesana, and Stephen R. Taylor. The Gravitational Wave Background from Massive Black Hole Binaries in Illustris: spectral features and time to detection with pulsar timing arrays. Mon. Not. Roy. Astron. Soc., 471(4):4508–4526, 2017.
- [22] Alessandra Buonanno, Gunter Sigl, Georg G. Raffelt, Hans-Thomas Janka, and Ewald Muller. Stochastic gravitational wave background from cosmological supernovae. Phys. Rev. D, 72:084001, 2005.
- [23] K. Crocker, V. Mandic, T. Regimbau, K. Belczynski, W. Gladysz, K. Olive, T. Prestegard, and E. Vangioni. Model of the stochastic gravitational-wave background due to core collapse to black holes. Phys. Rev. D, 92(6):063005, 2015.
- [24] Kyle Crocker, Tanner Prestegard, Vuk Mandic, Tania Regimbau, Keith Olive, and Elisabeth Vangioni. Systematic study of the stochastic gravitational-wave background due to stellar core collapse. Phys. Rev. D, 95(6):063015, 2017.
- [25] Pablo A. Rosado. Gravitational wave background from rotating neutron stars. Phys. Rev. D, 86:104007, 2012.
- [26] Paul D. Lasky, Mark F. Bennett, and Andrew Melatos. Stochastic gravitational wave background from hydrodynamic turbulence in differentially rotating neutron stars. Phys. Rev. D, 87(6):063004, 2013.
- [27] Dipongkar Talukder, Eric Thrane, Sukanta Bose, and Tania Regimbau. Measuring neutron-star ellipticity with measurements of the stochastic gravitational-wave background. Phys. Rev. D, 89(12):123008, 2014.
- [28] Kohei Inayoshi, Kazumi Kashiyama, Eli Visbal, and Zoltán Haiman. Gravitational wave background from Population III binary black holes consistent with cosmic reionization. Mon. Not. Roy. Astron. Soc., 461(3):2722–2727, 2016.
- [29] Michael S. Turner. Detectability of inflation produced gravitational waves. Phys. Rev. D, 55:435–439, 1997.
- [30] Neil Barnaby, Enrico Pajer, and Marco Peloso. Gauge Field Production in Axion Inflation: Consequences for Monodromy, non-Gaussianity in the CMB, and Gravitational Waves at Interferometers. Phys. Rev. D, 85:023525, 2012.
- [31] Jessica L. Cook and Lorenzo Sorbo. Particle production during inflation and gravitational waves detectable by ground-based interferometers. Phys. Rev. D, 85:023534, 2012. [Erratum: Phys.Rev.D 86, 069901 (2012)].
- [32] M. C. Guzzetti, N. Bartolo, M. Liguori, and S. Matarrese. Gravitational waves from inflation. Riv. Nuovo Cim., 39(9):399–495, 2016.
- [33] Richard Easther and Eugene A. Lim. Stochastic gravitational wave production after inflation. JCAP, 04:010, 2006.
- [34] Richard Easther, John T. Giblin, Jr., and Eugene A. Lim. Gravitational Wave Production At The End Of Inflation. Phys. Rev. Lett., 99:221301, 2007.
- [35] Juan Garcia-Bellido and Daniel G. Figueroa. A stochastic background of gravitational waves from hybrid preheating. Phys. Rev. Lett., 98:061302, 2007.
- [36] Paolo Campeti, Eiichiro Komatsu, Davide Poletti, and Carlo Baccigalupi. Measuring the

spectrum of primordial gravitational waves with CMB, PTA and Laser Interferometers. JCAP, 01:012, 2021.

- [37] M. Gasperini and G. Veneziano. Pre - big bang in string cosmology. Astropart. Phys., 1:317–339, 1993.
- [38] Vuk Mandic and Alessandra Buonanno. Accessibility of the pre-big-bang models to ligo. Phys. Rev. D, 73:063008, 2006.
- [39] M. Gasperini. Observable gravitational waves in pre-big bang cosmology: an update. JCAP, 12:010, 2016.
- [40] Thibault Damour and Alexander Vilenkin. Gravitational radiation from cosmic (super)strings: Bursts, stochastic background, and observational windows. Phys. Rev. D, 71:063510, 2005.
- [41] Xavier Siemens, Vuk Mandic, and Jolien Creighton. Gravitational wave stochastic background from cosmic (super)strings. Phys. Rev. Lett., 98:111101, 2007.
- [42] Uros Seljak and Anze Slosar. B polarization of cosmic microwave background as a tracer of strings. Phys. Rev. D, 74:063523, 2006.
- [43] Misao Sasaki, Teruaki Suyama, Takahiro Tanaka, and Shuichiro Yokoyama. Primordial black holes—perspectives in gravitational wave astronomy. Class. Quant. Grav., 35(6):063001, 2018.
- [44] Tomohiro Nakama, Joseph Silk, and Marc Kamionkowski. Stochastic gravitational waves associated with the formation of primordial black holes. Phys. Rev. D, 95(4):043511, 2017.
- [45] N. Bartolo, D. Bertacca, V. De Luca, G. Franciolini, S. Matarrese, M. Peloso, A. Ricciardone, A. Riotto, and G. Tasinato. Gravitational wave anisotropies from primordial black holes. JCAP, 02:028, 2020.
- [46] Arthur Kosowsky, Michael S. Turner, and Richard Watkins. Gravitational waves from first-order cosmological phase transitions. Phys. Rev. Lett., 69:2026–2029, Oct 1992.
- [47] Marc Kamionkowski, Arthur Kosowsky, and Michael S. Turner. Gravitational radiation from first order phase transitions. Phys. Rev. D, 49:2837–2851, 1994.
- [48] Carlo Baccigalupi, Luca Amendola, Pierluigi Fortini, and Franco Occhionero. The Stochastic gravitational background from inflationary phase transitions. Phys. Rev. D, 56:4610–4617, 1997.
- [49] Pierre Binetruy, Alejandro Bohe, Chiara Caprini, and Jean-Francois Dufaux. Cosmological Backgrounds of Gravitational Waves and eLISA/NGO: Phase Transitions, Cosmic Strings and Other Sources. JCAP, 06:027, 2012.
- [50] Chiara Caprini and Ruth Durrer. Gravitational wave production: A Strong constraint on primordial magnetic fields. Phys. Rev. D, 65:023517, 2001.
- [51] Daniela Paoletti and Fabio Finelli. Constraints on primordial magnetic fields from magnetically-induced perturbations: current status and future perspectives with LiteBIRD and future ground based experiments. JCAP, 11:028, 2019.
- [52] A. Buikema et al. Sensitivity and performance of the advanced ligo detectors in the third observing run. Phys. Rev. D, 102:062003, Sep 2020.
- [53] F. Acernese et al. Advanced Virgo: a second-generation interferometric gravitational wave detector. Class. Quant. Grav., 32(2):024001, 2015.
- [54] Kentaro Somiya. Detector configuration of KAGRA: The Japanese cryogenic gravitational-wave detector. Class. Quant. Grav., 29:124007, 2012.
- [55] B. Sathyaprakash et al. Scientific Objectives of Einstein Telescope. Class. Quant. Grav., 29:124013, 2012. [Erratum: Class.Quant.Grav. 30, 079501 (2013)].

- [56] Tania Regimbau et al. A Mock Data Challenge for the Einstein Gravitational-Wave Telescope. *Phys. Rev. D*, 86:122001, 2012.
- [57] Michele Maggiore et al. Science Case for the Einstein Telescope. *JCAP*, 03:050, 2020.
- [58] S. Hild et al. Sensitivity Studies for Third-Generation Gravitational Wave Observatories. *Class. Quant. Grav.*, 28:094013, 2011.
- [59] Giorgio Mentasti and Marco Peloso. ET sensitivity to the anisotropic Stochastic Gravitational Wave Background. 10 2020.
- [60] David Reitze et al. Cosmic Explorer: The U.S. Contribution to Gravitational-Wave Astronomy beyond LIGO. *Bull. Am. Astron. Soc.*, 51(7):035, 2019.
- [61] Stanislav Babak, Jonathan Gair, Alberto Sesana, Enrico Barausse, Carlos F. Sopuerta, Christopher P. L. Berry, Emanuele Berti, Pau Amaro-Seoane, Antoine Petiteau, and Antoine Klein. Science with the space-based interferometer LISA. V: Extreme mass-ratio inspirals. *Phys. Rev. D*, 95(10):103012, 2017.
- [62] Nicola Bartolo, Valerie Domcke, Daniel G. Figueroa, Juan García-Bellido, Marco Peloso, Mauro Pieroni, Angelo Ricciardone, Mairi Sakellariadou, Lorenzo Sorbo, and Gianmassimo Tasinato. Probing non-Gaussian Stochastic Gravitational Wave Backgrounds with LISA. *JCAP*, 11:034, 2018.
- [63] Alberto Sesana et al. Unveiling the Gravitational Universe at μ -Hz Frequencies. 8 2019.
- [64] Vishal Baibhav et al. Probing the Nature of Black Holes: Deep in the mHz Gravitational-Wave Sky. 8 2019.
- [65] Jeff Crowder and Neil J. Cornish. Beyond LISA: Exploring future gravitational wave missions. *Phys. Rev. D*, 72:083005, 2005.
- [66] Tristan L. Smith and Robert Caldwell. Sensitivity to a Frequency-Dependent Circular Polarization in an Isotropic Stochastic Gravitational Wave Background. *Phys. Rev. D*, 95(4):044036, 2017.
- [67] Naoki Seto, Seiji Kawamura, and Takashi Nakamura. Possibility of direct measurement of the acceleration of the universe using 0.1-Hz band laser interferometer gravitational wave antenna in space. *Phys. Rev. Lett.*, 87:221103, 2001.
- [68] Seiji Kawamura et al. Current status of space gravitational wave antenna DECIGO and B-DECIGO. 6 2020.
- [69] Manuel Arca Sedda et al. The missing link in gravitational-wave astronomy: discoveries waiting in the decihertz range. *Class. Quant. Grav.*, 37(21):215011, 2020.
- [70] Yousef Abou El-Neaj et al. AEDGE: Atomic Experiment for Dark Matter and Gravity Exploration in Space. *EPJ Quant. Technol.*, 7:6, 2020.
- [71] Zaven Arzoumanian et al. The NANOGrav 12.5 yr Data Set: Search for an Isotropic Stochastic Gravitational-wave Background. *Astrophys. J. Lett.*, 905(2):L34, 2020.
- [72] L. Lentati et al. European Pulsar Timing Array Limits On An Isotropic Stochastic Gravitational-Wave Background. *Mon. Not. Roy. Astron. Soc.*, 453(3):2576–2598, 2015.
- [73] Paul D. Lasky et al. Gravitational-wave cosmology across 29 decades in frequency. *Phys. Rev. X*, 6(1):011035, 2016.
- [74] A. Weltman et al. Fundamental physics with the Square Kilometre Array. *Publ. Astron. Soc. Austral.*, 37:e002, 2020.
- [75] Tania Regimbau. The astrophysical gravitational wave stochastic background. *Res. Astron. Astrophys.*, 11:369–390, 2011.

- [76] Pablo A. Rosado. Gravitational wave background from binary systems. Phys. Rev. D, 84:084004, 2011.
- [77] S. Marassi, R. Schneider, G. Corvino, V. Ferrari, and S. Portegies Zwart. Imprint of the merger and ring-down on the gravitational wave background from black hole binaries coalescence. Phys. Rev. D, 84:124037, 2011.
- [78] Xing-Jiang Zhu, E. Howell, T. Regimbau, D. Blair, and Zong-Hong Zhu. Stochastic Gravitational Wave Background from Coalescing Binary Black Holes. Astrophys. J., 739:86, 2011.
- [79] Xing-Jiang Zhu, Eric J. Howell, David G. Blair, and Zong-Hong Zhu. On the gravitational wave background from compact binary coalescences in the band of ground-based interferometers. Mon. Not. Roy. Astron. Soc., 431(1):882–899, 2013.
- [80] C. Wu, V. Mandic, and T. Regimbau. Accessibility of the Gravitational-Wave Background due to Binary Coalescences to Second and Third Generation Gravitational-Wave Detectors. Phys. Rev. D, 85:104024, 2012.
- [81] Kowalska-Leszczynska, I., Regimbau, T., Bulik, T., Dominik, M., and Belczynski, K. Effect of metallicity on the gravitational-wave signal from the cosmological population of compact binary coalescences. A&A, 574:A58, 2015.
- [82] B.P. Abbott et al. GW150914: Implications for the stochastic gravitational wave background from binary black holes. Phys. Rev. Lett., 116(13):131102, 2016.
- [83] Benjamin P. Abbott et al. GW170817: Implications for the Stochastic Gravitational-Wave Background from Compact Binary Coalescences. Phys. Rev. Lett., 120(9):091101, 2018.
- [84] Giulia Cusin, Cyril Pitrou, and Jean-Philippe Uzan. Anisotropy of the astrophysical gravitational wave background: Analytic expression of the angular power spectrum and correlation with cosmological observations. Phys. Rev. D, 96(10):103019, 2017.
- [85] Giulia Cusin, Cyril Pitrou, and Jean-Philippe Uzan. The signal of the gravitational wave background and the angular correlation of its energy density. Phys. Rev. D, 97(12):123527, 2018.
- [86] Giulia Cusin, Irina Dvorkin, Cyril Pitrou, and Jean-Philippe Uzan. First predictions of the angular power spectrum of the astrophysical gravitational wave background. Phys. Rev. Lett., 120:231101, 2018.
- [87] Giulia Cusin, Irina Dvorkin, Cyril Pitrou, and Jean-Philippe Uzan. Properties of the stochastic astrophysical gravitational wave background: astrophysical sources dependencies. Phys. Rev. D, 100(6):063004, 2019.
- [88] Giulia Cusin, Irina Dvorkin, Cyril Pitrou, and Jean-Philippe Uzan. Stochastic gravitational wave background anisotropies in the mHz band: astrophysical dependencies. MNRAS, 4 2019.
- [89] David Alonso, Giulia Cusin, Pedro G. Ferreira, and Cyril Pitrou. Detecting the anisotropic astrophysical gravitational wave background in the presence of shot noise through cross-correlations. Phys. Rev. D, 102(2):023002, 2020.
- [90] Alexander C. Jenkins and Mairi Sakellariadou. Anisotropies in the stochastic gravitational-wave background: Formalism and the cosmic string case. Phys. Rev. D, 98(6):063509, 2018.
- [91] Alexander C. Jenkins, Mairi Sakellariadou, Tania Regimbau, and Eric Slezak. Anisotropies in the astrophysical gravitational-wave background: Predictions for the detection of compact binaries by LIGO and Virgo. Phys. Rev. D, 98(6):063501, 2018.
- [92] Alexander C. Jenkins, Richard O’Shaughnessy, Mairi Sakellariadou, and Daniel Wysocki. Anisotropies in the astrophysical gravitational-wave background: The impact of black hole distributions. Phys. Rev. Lett., 122(11):111101, 2019.

- [93] Alexander C. Jenkins, Joseph D. Romano, and Mairi Sakellariadou. Estimating the angular power spectrum of the gravitational-wave background in the presence of shot noise. Phys. Rev. D, 100(8):083501, 2019.
- [94] Alexander C. Jenkins and Mairi Sakellariadou. Shot noise in the astrophysical gravitational-wave background. Phys. Rev. D, 100(6):063508, 2019.
- [95] Daniele Bertacca, Angelo Ricciardone, Nicola Bellomo, Alexander C. Jenkins, Sabino Matarrese, Alvise Raccanelli, Tania Regimbau, and Mairi Sakellariadou. Projection effects on the observed angular spectrum of the astrophysical stochastic gravitational wave background. Phys. Rev. D, 101(10):103513, 2020.
- [96] Cyril Pitrou, Giulia Cusin, and Jean-Philippe Uzan. Unified view of anisotropies in the astrophysical gravitational-wave background. Phys. Rev. D, 101(8):081301, 2020.
- [97] L. Boco, A. Lapi, S. Goswami, F. Perrotta, C. Baccigalupi, and L. Danese. Merging Rates of Compact Binaries in Galaxies: Perspectives for Gravitational Wave Detections. The Astrophysical Journal, 7 2019.
- [98] Giulio Scelfo, Lumen Boco, Andrea Lapi, and Matteo Viel. Exploring galaxies-gravitational waves cross-correlations as an astrophysical probe. JCAP, 7 2020.
- [99] Lumen Boco, Andrea Lapi, Martyna Chruslinska, Darko Donevski, Alex Sicilia, and Luigi Danese. Evolution of Galaxy Star Formation and Metallicity: Impact on Double Compact Objects Mergers. 12 2020.
- [100] Julien Lesgourgues. The cosmic linear anisotropy solving system (class) i: Overview, 2011.
- [101] Diego Blas, Julien Lesgourgues, and Thomas Tram. The cosmic linear anisotropy solving system (class). part ii: Approximation schemes. Journal of Cosmology and Astroparticle Physics, 2011(07):034–034, Jul 2011.
- [102] N. Aghanim et al. Planck 2018 results. VI. Cosmological parameters. Astron. Astrophys., 641:A6, 2020.
- [103] Martyna Chruslinska, Krzysztof Belczynski, Jakub Klencki, and Matthew Benacquista. Double neutron stars: merger rates revisited. Mon. Not. Roy. Astron. Soc., 474(3):2937–2958, 2018.
- [104] Michal Dominik, Krzysztof Belczynski, Christopher Fryer, Daniel E. Holz, Emanuele Berti, Tomasz Bulik, Ilya Mandel, and Richard O’Shaughnessy. Double compact objects. i. the significance of the common envelope on merger rates. The Astrophysical Journal, 759(1):52, 2012.
- [105] Nicola Giacobbo and Michela Mapelli. The progenitors of compact-object binaries: impact of metallicity, common envelope and natal kicks. Monthly Notices of the Royal Astronomical Society, 480(2):2011–2030, October 2018.
- [106] Martyna Chruslinska, Gijs Nelemans, and Krzysztof Belczynski. The influence of the distribution of cosmic star formation at different metallicities on the properties of merging double compact objects. Mon. Not. Roy. Astron. Soc., 482(4):5012–5017, 2019.
- [107] C. Mancuso, A. Lapi, J. Shi, J. Gonzalez-Nuevo, R. Aversa, and L. Danese. The Quest for Dusty Star-forming Galaxies at High Redshift $z \gtrsim 4$. Astrophys. J., 823(2):128, 2016.
- [108] F. Mannucci, G. Cresci, R. Maiolino, A. Marconi, and A. Gnerucci. A fundamental relation between mass, star formation rate and metallicity in local and high-redshift galaxies. Monthly Notices of the Royal Astronomical Society, 408(4):2115–2127, Sep 2010.
- [109] F. Mannucci, R. Salvaterra, and M. A. Campisi. The metallicity of the long grb hosts and the fundamental metallicity relation of low-mass galaxies. Monthly Notices of the Royal Astronomical Society, 414(2):1263–1268, Mar 2011.

- [110] Leslie Hunt, Pratika Dayal, Laura Magrini, and Andrea Ferrara. Coevolution of metallicity and star formation in galaxies to $z \simeq 3.7$ – ii. a theoretical model. Monthly Notices of the Royal Astronomical Society, 463(2):2020–2031, Aug 2016.
- [111] Mirko Curti, Filippo Mannucci, Giovanni Cresci, and Roberto Maiolino. The mass–metallicity and the fundamental metallicity relation revisited on a fully te-based abundance scale for galaxies. Monthly Notices of the Royal Astronomical Society, 491(1):944–964, Nov 2019.
- [112] E. et al. Daddi. Multiwavelength Study of Massive Galaxies at $z \sim 2$. II. Widespread Compton-thick Active Galactic Nuclei and the Concurrent Growth of Black Holes and Bulges. The Astrophysical Journal, 670(1):173–189, November 2007.
- [113] G. et al. Rodighiero. The Lesser Role of Starbursts in Star Formation at $z = 2$. ApJ Letter, 739(2):L40, October 2011.
- [114] G. et al. Rodighiero. Relationship between Star Formation Rate and Black Hole Accretion At $Z = 2$: the Different Contributions in Quiescent, Normal, and Starburst Galaxies. ApJ Letter, 800(1):L10, February 2015.
- [115] Katherine E. et al. Whitaker. Constraining the Low-mass Slope of the Star Formation Sequence at $0.5 < z < 2.5$. The Astrophysical Journal, 795(2):104, November 2014.
- [116] J. S. Speagle, C. L. Steinhardt, P. L. Capak, and J. D. Silverman. A Highly Consistent Framework for the Evolution of the Star-Forming “Main Sequence” from $z \sim 0$ –6. The Astrophysical Journal Supplement Series, 214(2):15, October 2014.
- [117] C. et al. Schreiber. The Herschel view of the dominant mode of galaxy growth from $z = 4$ to the present day. Astronomy and Astrophysics, 575:A74, March 2015.
- [118] J. S. et al. Dunlop. A deep ALMA image of the Hubble Ultra Deep Field. Monthly Notices of the Royal Astronomical Society, 466(1):861–883, April 2017.
- [119] R. Abbott et al. Population Properties of Compact Objects from the Second LIGO-Virgo Gravitational-Wave Transient Catalog. 10 2020.
- [120] Lee Samuel Finn. Binary inspiral, gravitational radiation, and cosmology. Phys. Rev. D, 53:2878–2894, 1996.
- [121] Stephen R. Taylor and Jonathan R. Gair. Cosmology with the lights off: standard sirens in the Einstein Telescope era. Phys. Rev. D, 86:023502, 2012.
- [122] P. Ajith et al. A Template bank for gravitational waveforms from coalescing binary black holes. I. Non-spinning binaries. Phys. Rev. D, 77:104017, 2008. [Erratum: Phys.Rev.D 79, 129901 (2009)].
- [123] Enea Di Dio, Francesco Montanari, Julien Lesgourgues, and Ruth Durrer. The CLASSgal code for Relativistic Cosmological Large Scale Structure. JCAP, 11:044, 2013.
- [124] Camille Bonvin and Ruth Durrer. What galaxy surveys really measure. Physical Review D, 84(6), Sep 2011.
- [125] Anthony Challinor and Antony Lewis. Linear power spectrum of observed source number counts. Physical Review D, 84(4), Aug 2011.
- [126] R. Aversa, A. Lapi, G. de Zotti, F. Shankar, and L. Danese. Black Hole and Galaxy Coevolution from Continuity Equation and Abundance Matching. Astrophys. J., 810(1):74, 2015.
- [127] Ravi K. Sheth, H.J. Mo, and Giuseppe Tormen. Ellipsoidal collapse and an improved model for the number and spatial distribution of dark matter haloes. Mon. Not. Roy. Astron. Soc., 323:1, 2001.
- [128] A. Lapi and L. Danese. Statistics of Dark Matter Halos in the Excursion Set Peak Framework. JCAP, 07:044, 2014.

- [129] Lam Hui, Enrique Gaztañaga, and Marilena LoVerde. Anisotropic magnification distortion of the 3d galaxy correlation. i. real space. Physical Review D, 76(10), Nov 2007.
- [130] Giulio Scelfo, Nicola Bellomo, Alvise Raccanelli, Sabino Matarrese, and Licia Verde. GW×LSS: chasing the progenitors of merging binary black holes. JCAP, 09:039, 2018.
- [131] A. Lapi, M. Negrello, J. González-Nuevo, Z.-Y. Cai, G. De Zotti, and L. Danese. Effective models for statistical studies of galaxy-scale gravitational lensing. The Astrophysical Journal, 755(1):46, Jul 2012.
- [132] J. Gonzalez-Nuevo, L. Toffolatti, and F. Argueso. Predictions of the angular power spectrum of clustered extragalactic point sources at cosmic microwave background frequencies from flat and all-sky two-dimensional simulations. The Astrophysical Journal, 621(1):1–14, mar 2005.
- [133] Andrea Zonca, Leo Singer, Daniel Lenz, Martin Reinecke, Cyrille Rosset, Eric Hivon, and Krzysztof Gorski. healpy: equal area pixelization and spherical harmonics transforms for data on the sphere in python. Journal of Open Source Software, 4(35):1298, March 2019.
- [134] K. M. Górski, E. Hivon, A. J. Banday, B. D. Wandelt, F. K. Hansen, M. Reinecke, and M. Bartelmann. HEALPix: A Framework for High-Resolution Discretization and Fast Analysis of Data Distributed on the Sphere. ApJ, 622:759–771, April 2005.
- [135] Guadalupe Cañas Herrera, Omar Contigiani, and Valeri Vardanyan. Cross-correlation of the astrophysical gravitational-wave background with galaxy clustering. Phys. Rev. D, 102(4):043513, 2020.